Computational Fluid Dynamics Simulation of Steam Reforming and Autothermal Reforming for Fuel Cell Applications

A thesis presented to

the faculty of

the Russ College of Engineering and Technology of Ohio University

In partial fulfillment

of the requirements for the degree

Master of Science

Liming Shi

March 2009

© 2009 Liming Shi. All Rights Reserved.

This thesis titled

Computational Fluid Dynamics Simulation of Steam Reforming and Autothermal Reforming for Fuel Cell Applications

by

LIMING SHI

has been approved for

the Department of Chemical and Biomolecular Engineering

and the Russ College of Engineering and Technology by

Michael E. Prudich

Professor, Department of Chemical and Biomolecular Engineering

Dennis Irwin

Dean, Russ College of Engineering and Technology

ABSTRACT

SHI, LIMING, M.S., March 2009, Chemical Engineering

Computational Fluid Dynamics Simulation of Steam Reforming and Autothermal Reforming for Fuel Cell Applications (104 pp.)

Director of Thesis: Michael E. Prudich

With the increasing demand for fuel cell applications in transportation, the performance of reformers using gasoline or diesel as the fuel needs to be optimized. Numerical models based on computational fluid dynamics (CFD) were used to simulate the performance of these reformers. A CFD model of steam reforming and a CFD model of autothermal reforming were developed and validated for two reformers. Each model included submodels for the reactor and reaction chemistry. A single channel was used in the model of steam reforming and a whole reactor was modeled in the model of autothermal reforming. A reaction rate expression was developed for the steam reforming reaction to form hydrogen and carbon dioxide. The CFD results provided an adequate match to the experimental data from the literature. The percentage of difference between each experimental measurement of the mole fraction of hydrogen and the corresponding CFD prediction was less than 17.7% for the model of steam reforming and 16.8% for the model of autothermal reforming. The CFD models were used to predict reformer performance. For steam reforming, the inlet steam-to-carbon molar ratio had a negligible effect on reforming efficiency when it was varied from 2 to 4. The reforming efficiency decreased slightly as the inlet velocity was increased from 2.9 to 8.7 m/s, which was mainly caused by the steam reforming reaction. For autothermal reforming, the thermal conductivity of the catalyst support affected the temperature profile in the reactor, but its effect on the mole fraction of hydrogen in the products was negligible. The reforming efficiency decreased by 11.5% as power input was increased from 1.7 to 8.4 kW.

Approved: ____

Michael E. Prudich

Professor, Department of Chemical and Biomolecular Engineering

ACKNOWLEDGMENTS

I would like to thank my thesis advisor Professor Michael Prudich for his valuable guidance and inspiring discussions. I would also like to thank the members of my thesis committee, Dr. Martin Mohlenkamp, Dr. Ben Stuart, and Dr. Kevin Crist, for their time and help. I am particularly grateful to Professor David Bayless for his financial support and encouragement during this study. Finally, I would especially like to thank my husband, my daughter, and my parents for their love and care.

TABLE OF CONTENTS

Page

LIST OF TABLES

LIST OF FIGURES

Page

CHAPTER 1: INTRODUCTION

This chapter gives an overview of background, significance of this research, and research objectives.

1.1 Background

Fuel cells directly convert the chemical energy of a fuel into electrical energy. For a solid oxide fuel cell (SOFC), oxygen is reduced to oxygen ions at the cathode, the oxygen ions move to the anode through an electrolyte, and react with a fuel, like hydrogen, at the anode to release electrons, heat, and water [1].

The United States consumes billions of gallons of gasoline each year in transportation. For example, the U.S. total gasoline sales were 377,000 thousand gallons per day in 2006 [2]. The efficiency of a fuel cell system is about 40-60% [3] while that of a conventional internal combustion engine is only around 20% [4]. Therefore, the application of fuel cell systems in transportation has the potential to improve energy efficiencies and reduce pollutant emissions [5].

Two types of fuel cells, the proton exchange membrane fuel cell (PEMFC) and the solid oxide fuel cell (SOFC), are suitable for application to transportation. The PEMFC can only use hydrogen as fuel and its operating temperature is low (70 °C). Carbon monoxide is a poison to the catalyst of a PEMFC anode. In contrast, SOFCs operate at high temperatures (about 800-1000 °C), and both H_2 and CO can be oxidized at its anode. The fuel processing system for SOFCs is relatively simpler than that for PEMFCs because it does not need additional separation to remove CO [3].

Fuel cells consume fuel continuously. Hydrogen is a desirable fuel for fuel cells, but a current infrastructure for H_2 production, storage, and distribution is not available. In the near future, a practical method for the production of hydrogen may involve an on-board reformer using gasoline, diesel, or other petroleum-based liquid fuel as hydrogen carriers. The power generation system is a combination of a fuel reformer and fuel cells. Much research has been done to investigate fuel reforming, both experimentally and theoretically. Many theoretical investigations have used the thermodynamic equilibrium method to predict the product compositions expected from a reformer.

Generally, there are three methods of fuel reforming, which include steam reforming (SR), partial oxidation (PO), and autothermal reforming (ATR). Steam reforming is endothermic. Partial oxidation is exothermic. The ratio of oxygen to fuel for PO is lower than that required at complete combustion. Catalytic partial oxidation (CPO) is commonly used to lower the reaction temperature. The reactants for autothermal reforming include steam, oxygen, and fuel. Autothermal reforming is a combination of SR and PO. Brown [6] compared these three reforming methods and concluded that both partial oxidation and autothermal reforming are the preferred methods for an on-board reformer because they are both net exothermic and, as such, do not require an additional heat source in a vehicle. This study focused on computational fluid dynamics (CFD) simulations of the performance of fuel reformers.

1.2 Significance of the Research

The primary objective of this research is to numerically study fuel reforming processes using three-dimensional (3D) CFD. Simulation results can provide profiles of velocity, temperature, and species concentrations at every point in the reforming reactor. The deviation of each point from the root-mean-square (RMS) value of a cross section can be determined. This information is useful in the system design to avoid problems like hot spots, which can destroy the catalyst, because catalyst activity is sensitive to temperature. Therefore, CFD simulation can help optimize the design of the reactor and identify conditions which can improve the fuel conversion efficiency. It can also reduce time and cost to implement new ideas and designs.

Methane has been used as the fuel in many experimental and modeling studies of fuel processing. The reforming processes using gasoline or diesel are less understood than those using methane. To model the processes using gasoline or diesel, a reaction mechanism and kinetics must be provided. Therefore, CFD simulation can help to gain insight into the reaction chemistry.

Because the U.S. consumes billions of gallons of gasoline each year, any improvement in fuel-use efficiency can save a significant amount of fuel. A decrease in fuel usage naturally leads to a simultaneous reduction in pollutant emissions. The significance of this research is apparent because the results will be useful to the improvement of the reforming efficiency.

1.3 Objectives

The objective of this research is to simulate steam reforming and autothermal reforming with fuels of gasoline or diesel using CFD. Both gasoline and diesel are blends of different hydrocarbons. They are usually represented by one or two hydrocarbons in a theoretical analysis. They are the fuels in favor because an infrastructure currently exists for their supply and distribution. In this study, iso-octane was used as a surrogate for gasoline and n-hexadecane was used as a surrogate for diesel fuel.

First, two models were built and validated for two different reformers. One was a single channel in an isothermal flat-bed reactor for the steam reforming of iso-octane and the other was the whole reactor in a type of monolith for the autothermal reforming of n-hexadecane. Each model consisted of a reactor model in 3D which included the conservation equations of mass, momentum, energy, and species, and a reaction chemistry model which included reaction mechanisms and kinetics. These reforming process/reactor type/fuel combinations were selected for CFD simulations due to the fact that experimental results were available from the literature which could be used for model validation.

The second objective was to investigate the effect of varying operating parameters on the H_2 yield and reforming efficiency. The operating parameters studied included the inlet steam-to-carbon molar ratio (H_2O/C), gas velocity at the reactor inlet, thermal conductivity of the catalyst support, and power input (feed fuel flow rate). The distributions of temperature, species concentration, and velocity were calculated.

CHAPTER 2: LITERATURE REVIEW

This chapter reviews the current research about fuel reforming. It includes a review of reforming methods, models for the reactor, reaction mechanisms and kinetics, modeling work, and experimental work.

The basics of fuel reforming have been investigated intensively. This study focuses on the CFD modeling of fuel reformers to predict its performance. A small-scale power system (1-100 kW) is shown in Figure 2.1 (Krumpelt et al. [3]). It consists of a catalytic reformer, a SOFC stack, a combustor and air preheater. Fuel is pumped into the reformer. The most promising catalysts for reforming are transition metals, such as nickel and rhodium. Part of the exhaust gases from the anode of the SOFC are sent to the inlet of the reformer, and part to the combustor. Air is preheated before entering into the reformer or the cathode of the SOFC.

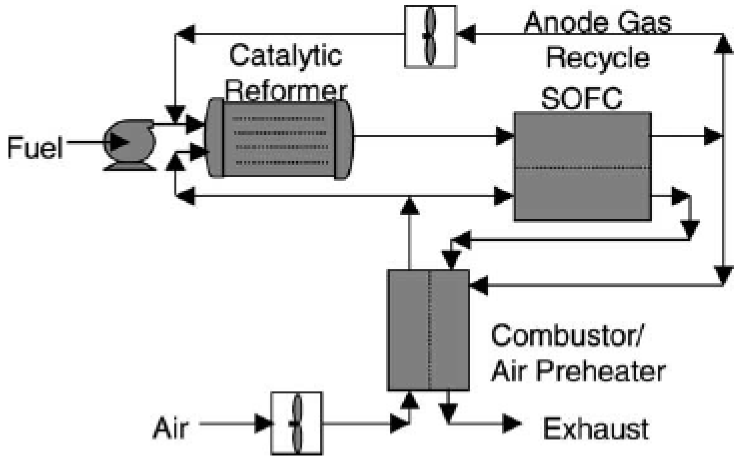

Figure 2.1. Schematic of a SOFC-based power system [3].

2.1 Reforming Methods

2.1.1 Steam Reforming

In steam reforming (SR), a fuel reacts with high temperature steam. The reaction for a hydrocarbon (C_nH_m) is

$$C_nH_m\ (l) + n\ H_2O\ (g) \leftrightarrow n\ CO\ (g) + (\frac{m}{2} + n)\ H_2\ (g) \tag{2.1}$$

The water gas shift (WGS) reaction also occurs. The WGS reaction can be described as

$$CO + H_2O \leftrightarrow CO_2 + H_2 \tag{2.2}$$

Steam reforming is highly endothermic. If C_nH_m represents iso-octane (n = 8, m = 18), a surrogate for gasoline, the required heat input for Equation (2.1) is 1309.62 kJ/mol C_8H_{18} at 25 ˚C. A certain fraction of the heat is used to evaporate the liquid fuel.

2.1.2 Partial Oxidation

Partial oxidation of hydrocarbons for H_2 production requires high temperatures. Catalysts are commonly used in partial oxidation to help reduce the operating temperature and to produce practical reaction rates [7]. Possible reactions include

$$C_nH_m\ (l) + \frac{n}{2}\ O_2\ (g) \rightarrow n\ CO\ (g) + \frac{m}{2}\ H_2\ (g) \tag{2.3}$$

$$C_nH_m\ (l) + n\ O_2\ (g) \rightarrow n\ CO_2\ (g) + \frac{m}{2}\ H_2\ (g) \tag{2.4}$$

These reactions are both exothermic. If C_nH_m represents iso-octane, the heat released is 624.94 kJ/mol C_8H_{18} for Equation (2.3) and 2888.86 kJ/mol C_8H_{18} for Equation (2.4) at 25 ˚C. For partial oxidation, the amount of oxygen supplied is not enough for complete combustion. Solid carbon deposition, which may be caused by the Boudouard reaction or methane cracking, should be avoided because this will significantly affect the performance of the catalyst.

2.1.3 Autothermal Reforming

Autothermal reforming (ATR) is the combination of steam reforming and partial oxidation. The reactions include those happening both with SR and PO (Equations 2.1 through 2.4). Autothermal reforming is a self-sustaining process. The heat released from PO is used to provide the heat required by SR. The net amount of heat generated from ATR reactions is close to or slightly above zero. Because CO can be used as a fuel for SOFCs, preferential oxidation can be eliminated since its purpose is to convert CO to CO_2.

2.2 Reactor Models

There are a variety of models for catalytic reactor systems [8-9], which can be classified by their modeled dimensions. The one-dimensional (1D) model [10] calculates the profile of variables along the axial direction of the reactor and ignores radial variation. It consists of mass and energy balance equations for the gas and solid phases. Average velocity is used for each location. The 1D model used by most researchers does not include an equation for velocity calculation, while velocity is simulated in CFD-based models.

To study spatial profiles, several two-dimensional (2D) models based on boundary layer formulations [11-12] or Navier-Stokes equations [13] have been developed. The boundary layer model used is relatively simple. It assumes that axial diffusion is negligible. Researchers have also implemented 3D models for monolith reactors [14-15]. These 3D models include equations for mass, momentum, energy, and species. The results are used to validate the simpler models. The major part of the reactor is the catalyst substrate. Figure 2.2 shows several catalyst substrates as presented in Giroux et al. [16]. The catalyst support material is either ceramic or metallic. The active catalyst is coated on the geometric surface of the support.

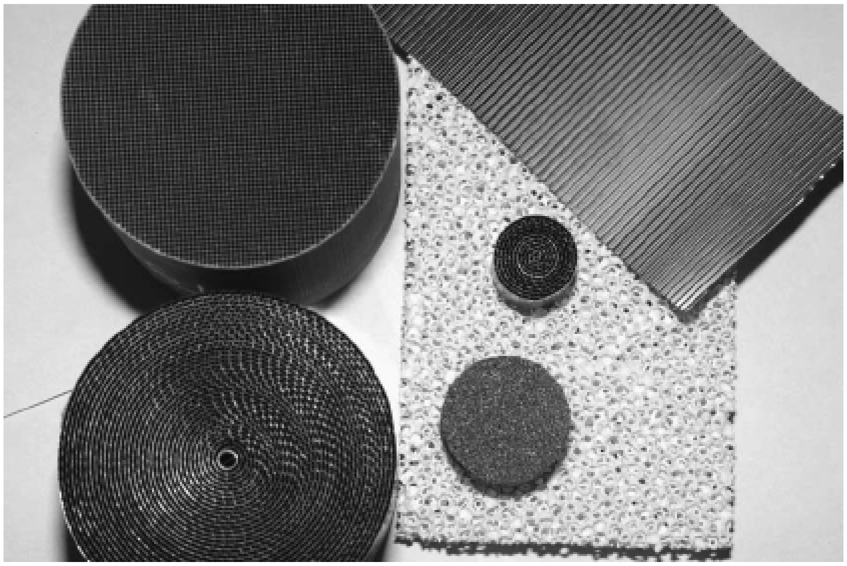

Figure 2.2. Picture of six types of catalyst substrates (clockwise from lower left): large metal monolith, ceramic monolith, corrugated metal foil sheet, small metal monolith, fine metal foam (bottom), small coarse ceramic foam [16].

2.3 Reaction Mechanism

The elementary chemical reaction steps for the reforming of higher hydrocarbons are unknown. The overall reaction is usually used to describe the process. There are investigations about the detailed reaction mechanism for methane combustion. For example, the group of Deuthmann [17] derived a reaction mechanism for methane partial oxidation on platinum catalyst. This mechanism consists of more than 100 elementary reactions and includes 30 species. These numbers would be expected to be much higher for hydrocarbons with carbon numbers greater than one. Simulations involving a complete set of elementary reactions would be difficult to converge and computationally expensive. It is known that only a few reactions are rate limiting. Most of the other reactions can be ignored. It has been found that a simplified reaction mechanism can be sufficient to accurately predict the product concentrations at the outlet of the reactor. Therefore, a simplified reaction mechanism was used in this work. The simplified mechanism included several reactions and species.

For the simulation of methane reforming, De Groote and Froment [18] proposed a reaction mechanism which included nine reactions. They are listed as follows:

Complete combustion: $CH_4 + 2\ O_2 \rightarrow CO_2 + 2\ H_2O$ (2.5)

Steam reforming: $CH_4 + H_2O \leftrightarrow CO + 3\ H_2$ (2.6)

$CH_4 + 2\ H_2O \leftrightarrow CO_2 + 4\ H_2$ (2.7)

Water gas shift reaction: $CO + H_2O \leftrightarrow CO_2 + H_2$ (2.2)

CO_2 reforming: $CH_4 + CO_2 \leftrightarrow 2\ CO + 2\ H_2$ (2.8)

Boudouard reaction: $2\ CO \leftrightarrow C + CO_2$ (2.9)

Methane cracking: $CH_4 \leftrightarrow C + 2\ H_2$ (2.10)

Carbon gasification by steam: $C + H_2O \leftrightarrow CO + H_2$ (2.11)

Carbon gasification by oxygen: $C + O_2 \rightarrow CO_2$ (2.12)

All the reactions are non-elementary. It can be seen that solid carbon is involved in the last four reactions. Because the amount of solid carbon present in the final product is usually very small, or zero, most modeling work ignores the last four reactions. For simulating hydrocarbons that are not methane, most researchers replace methane in the above reactions by the modeled hydrocarbon, appropriately adjusting the stoichiometries, but keeping the products the same.

Pacheco et al. [10] utilized the format of the first five reactions for the modeling of iso-octane reforming in a fixed-bed reactor using a ceria-oxide catalyst impregnated with platinum. The reactions were combustion, steam reforming with CO and CO_2 as the product, carbon dioxide reforming, and WGS.

$$C_8H_{18} + 16\ O_2 \rightarrow 8\ CO_2 + 9\ H_2O \tag{2.13}$$

$$C_8H_{18} + 8\ H_2O \leftrightarrow 8\ CO + 17\ H_2 \tag{2.14}$$

$$C_8H_{18} + 16\ H_2O \leftrightarrow 8\ CO_2 + 25\ H_2 \tag{2.15}$$

$$C_8H_{18} + 8\ CO_2 \leftrightarrow 16\ CO + 9\ H_2 \tag{2.16}$$

$$CO + H_2O \leftrightarrow CO_2 + H_2 \tag{2.2}$$

The reaction mechanism used by Hoang and Chan [19] for methane reforming consisted of the first four reactions. Moreover, Papadias et al. [20] used the format of three reactions (Equations 2.2, 2.5, 2.6) to describe gasoline reforming, similar to the assumption that Lattner and Harold [21] used to describe n-tetradecane reforming.

2.4 Reaction Kinetics

Reaction rate expressions are needed to describe the progress of the reactions given in the reaction mechanism. However, kinetics information about the reforming process is very limited. Among the available kinetics studies, two types of rate expressions are commonly used to describe the heterogeneous chemical reactions occurring on the catalytic surface. They are the power law model and the Langmuir–Hinshelwood–Hougen–Watson (LHHW) model.

There is not much kinetic data for heavy hydrocarbon reforming in the literature. Kinetic models have been derived mainly based on the experimental data available for methane reforming. Because of the lack of experimental data, the rate expressions for higher hydrocarbons used by many researchers [10, 20] are similar to those used for methane. The difference is in the rate constants, which are regressed based on the experimental data.

2.4.1 Kinetic Models for Steam Reforming

There are two frequently cited models for methane steam reforming. One was developed by Xu and Froment [22], and the other derived by Numaguchi and Kikuchi [23]. Xu and Froment [22] have investigated methane steam reforming over $Ni/MgAl_2O_4$ catalyst in a tubular reactor. The temperature was in the range of 500-575 °C and the pressure was between 3 and 15 bar. In their testing, H_2 was included in the feed to protect the Ni catalyst from re-oxidation by steam, but usually H_2 would not be added at the inlet. By comparing the experimental data with the equilibrium constants, three reactions were identified as the major reactions in the reforming process. They are the steam reforming reaction with CO (Equation 2.6) and CO_2 (Equation 2.7) as the products, and the WGS reaction (Equation 2.2). They proposed Langmuir–Hinshelwood (LH) type rate expressions for these reactions. These rate expressions are shown in Table 2.1.

Numaguchi and Kikuchi [23] conducted experiments on 8.7 wt% Ni/Al_2O_3 catalyst at 5–20% methane conversions in a fixed-bed reactor. The temperature was around 400–890 °C, the pressure was between 1.2 and 25.5 bar, and the inlet steam–to–CH_4 ratio was at 1.44–4.5. Their operating temperatures and pressures were higher than those tested by Xu and Froment [22]. They assumed that only CO was formed from the reaction between CH_4 and H_2O (Equation 2.6). Carbon dioxide was only produced from the WGS reaction. The rate-determining step was the surface reaction. Their reaction rate expressions are presented in Table 2.2.

Table 2.1. Reaction rate expressions by Xu and Froment [22]

Reactions	**Rate Expressions**
$CH_4 + H_2O \leftrightarrow CO + 3H_2$	$r_1 = \dfrac{k_1 / p_{H_2}^{2.5}(p_{CH_4}p_{H_2O} - p_{H_2}^3 p_{CO} / K_{eq,1})}{(1 + K_{CO}p_{CO} + K_{H_2}p_{H_2} + K_{CH_4}p_{CH_4} + K_{H_2O}p_{H_2O}/p_{H_2})^2}$
$CH_4 + 2H_2O \leftrightarrow CO_2 + 4H_2$	$r_2 = \dfrac{k_2 / p_{H_2}^{3.5}(p_{CH_4}p_{H_2O}^2 - p_{H_2}^4 p_{CO_2} / K_{eq,2})}{(1 + K_{CO}p_{CO} + K_{H_2}p_{H_2} + K_{CH_4}p_{CH_4} + K_{H_2O}p_{H_2O}/p_{H_2})^2}$
$CO + H_2O \leftrightarrow CO_2 + H_2$	$r_3 = \dfrac{k_3 / p_{H_2}(p_{CO}p_{H_2O} - p_{H_2} p_{CO_2} / K_{eq,3})}{(1 + K_{CO}p_{CO} + K_{H_2}p_{H_2} + K_{CH_4}p_{CH_4} + K_{H_2O}p_{H_2O}/p_{H_2})^2}$

Table 2.2. Reaction rate expressions by Numaguchi and Kikuchi [23]

Reactions	**Rate Expressions**
$CH_4 + H_2O \leftrightarrow CO + 3H_2$	$r_1 = \dfrac{k_1(p_{CH_4} - p_{H_2}^3 p_{CO} / K_{eq,1})}{p_{CH_4}^{\alpha_1} p_{H_2O}^{\beta_1}}$
$CO + H_2O \leftrightarrow CO_2 + H_2$	$r_2 = \dfrac{k_2(p_{CO} - p_{H_2} p_{CO_2} / K_{eq,2})}{p_{CH_4}^{\alpha_2} p_{H_2O}^{\beta_2}}$

where k_i and $K_{eq,i}$ represent the reaction rate coefficient and the overall partial pressure equilibrium constant (i = 1, 2, 3), respectively. K_i and p_i represent the adsorption equilibrium constant and the partial pressure (i = CO, H_2, CH_4, H_2O, CO_2), respectively. α_i and β_i are exponents (i = 1, 2).

The k_i (in the lower case) constants in the above tables can be calculated at different temperatures through the use of the Arrhenius equation $k_i = k_{i,0}\, e^{(-Ei/RT)}$, where $k_{i,0}$ is the pre-exponential factor. The kinetic data and the corresponding values of the constants derived from the methane conversion rate can be found in the corresponding references. Because both studies used small catalyst particles, there was no internal diffusion limitation during testing.

De Smet et al. [24] compared the influence of these two intrinsic kinetic models on the simulation of catalytic partial oxidation of methane in an adiabatic fixed-bed reactor using a steady-state 1D model. In general, the catalyst temperature predicted by the model of Xu and Froment was always lower than that predicted by the model of Numaguchi and Kikuchi at positions toward the inlet of the reactor, but both models predicted the same temperature at the end of the reactor.

2.4.2 Kinetic Models for Partial Oxidation

Trimm and Lam [25] derived a LH rate expression for the complete combustion of methane (Equation 2.5) on Pt/Al_2O_3 catalyst at temperature above 557 °C and inlet O_2/CH_4 ratios between 0.3 and 5. This expression is given in Equation (2.17).

$$r = \frac{k_a p_{CH_4} p_{O_2}}{(1 + K_{CH_4} p_{CH_4} + K_{O_2} p_{O_2})^2} + \frac{k_b p_{CH_4} p_{O_2}^{0.5}}{(1 + K_{CH_4} p_{CH_4} + K_{O_2} p_{O_2})} \tag{2.17}$$

The first term in the reaction rate equation represents the reaction between molecularly adsorbed methane and oxygen, and the second term accounts for the Eley-Rideal reaction between molecularly adsorbed methane and gaseous oxygen. De Smet et al. [24] changed the exponent of partial pressure of O_2 in the numerator from 0.5 to 1 in their work.

Ma et al. [26] studied the kinetics of oxidation of methane, ethane, and propane over a supported Pt catalyst. They derived a power law rate model and a LH model to describe the kinetics of methane oxidation. The reaction order with respect to oxygen is non-monotomic. The LH model was based on the reaction between adsorbed methane and molecules of atomic oxygen. They concluded that longer chain hydrocarbons are more reactive. The kinetic expressions were for temperatures over the range 360–460 °C.

The power law rate expression [26] is given as

$$r_{CH_4} = -\frac{d(C_{CH_4})}{dt} = k(C_{CH_4})^{0.95}(C_{O_2})^{-0.17} \tag{2.18}$$

where C_{CH4} and C_{O2} are concentrations of CH_4 and O_2, respectively.

The LH model expression [26] is given by

$$r_{CH_4} = -\frac{d(C_{CH_4})}{dt} = \frac{kK_{CH_4}p_{CH_4}\sqrt{K_{O_2}p_{O_2}}}{(1+K_{CH_4}p_{CH_4}+\sqrt{K_{O_2}p_{O_2}})^2} \tag{2.19}$$

where k is a reaction rate coefficient, and K_{CH4} and K_{O2} are adsorption coefficient for CH_4 and O_2, respectively.

Ibrahim and Idem [27] investigated the kinetics of the partial oxidation of iso-octane over a Ni/Al_2O_3 catalyst in a tubular fixed-bed reactor. The temperature was in the range of 590–640 °C, and the pressure was atmospheric. The overall reaction was given by

$$C_8H_{18} + 4\ O_2 \rightarrow 8\ CO + 9\ H_2 \qquad \Delta H_{298} = -660\ \text{kJ/mol} \tag{2.20}$$

It can be seen that only CO and H_2 were assumed to be the products of the partial oxidation reaction. Their theoretical calculations indicated that the experimental conditions were not limited by heat and mass transfer. The measured data was used for the calculation of the intrinsic kinetic rate.

One power law rate model, fourteen models based on LHHW, and two Eley-Rideal formulations were tested in comparison with the experimental data. They found that a power law model and one LHHW type model gave good predictions. The LHHW type model exhibited the best fit of the experimental data. The mechanism for this model required the dissociative adsorption of C_8H_{18}, the molecular adsorption of O_2 on a single site, and surface reaction being the rate-determining step. The rate expression for this model [27] is given by

$$r_{C_8H_{18}} = \frac{k_0 e^{(-E/RT)} C_{C_8H_{18}}^{1.5}}{[1 + (K_A C_{C_8H_{18}})^{0.5} + K_B C_{C_8H_{18}}]^2} \tag{2.21}$$

where $k_0 = 1.25 \times 10^{23}$ 1/kg-cat·s, the activation energy $E = 2.82 \times 10^5$ J/mol, $K_A = 5.85 \times 10^{-4}$ $1/\text{mol}^{0.5}\cdot\text{m}^{1.5}$, and $K_B = 2.51 \times 10^7$ $\text{m}^{0.75}/\text{mol}^{0.75}$. C is in units of mol/m^3, resulting in r_{C8H18} in units of mol/kg·s.

The empirical power law model also gave very good estimations. The average absolute deviation from the experimental data was only 6.75%. The rate expression for this model [27] is given by

$$r_{C_8H_{18}} = k_0 e^{(-E/RT)} C_{C_8H_{18}}^{0.82} \tag{2.22}$$

where $k_0 = 4.33 \times 10^{18}$ 1/kg-cat/s, and $E = 2.99 \times 10^5$ J/mol.

2.4.3 Kinetic Models for WGS

In addition to the rate expressions for the WGS reaction given in Tables 2.1 and 2.2, the kinetics of the WGS reaction have been studied by many researchers [28-30]. According to Grenoble et al. [29], the reaction rate can be described by a power law expression of the form

$$r = kp_{co}^{x} p_{H_2O}^{(\frac{1-x}{2})} \tag{2.23}$$

The exponents of p_{CO} and p_{H2O} are determined by the active metals supported on the alumina. The value of x is in the range of -0.35 to +0.74.

Wheeler et al. [30] investigated the WGS reaction over noble metals (Pt, Rh, Ru) and metals (Ni, Pd) with ceria at short contact times (0.008-0.05 s) and temperatures between 300 and 1000 °C. It was found that a simple rate expression provided a good fit for all data at all temperatures from equilibrium conversion to low conversions. Their model was first order with respect to all species and is written as

$$r = k_f p_{CO} p_{H_2O} - k_b p_{CO_2} p_{H_2} \tag{2.24}$$

where k_f and k_b are the forward and backward rate constants, respectively.

2.4.4 Kinetic Models for ATR

Autothermal reforming is a combination of partial oxidation and steam reforming. According to the temperature distribution along the length of the reactor [31], it is clear that the exothermic reaction happens near the front end of the reactor. Partial oxidation happens first because its reaction rate is faster than that of steam reforming. Next, the products from oxidation and part of the fuel go through the steam reforming process. There is no agreement on the products that are formed from partial oxidation. Some investigators assume that these products are CO_2 and H_2O, while others assume that they are CO and H_2. The behavior of this reaction needs further investigation.

2.5 Modeling Work

This section gives an overview about the current status of modeling of reforming processes including steam reforming, partial oxidation, and autothermal reforming. A variety of reactors have been used for the modeling. All these models assumed that flow in the reactor is laminar. Many models were performed at the steady state.

Veser et al. [32] simulated catalytic methane oxidation over platinum in a monolith reactor. Their model contained one-dimensional mass and energy balance equations for the gas phase and the catalytic monolith. Because of the longer ignition delay of the homogeneous reaction, only reactions occurring on the catalyst surface were considered. The reaction was actually limited by the reactant adsorption onto the catalyst surface. Therefore, the mass-transfer limitation in the boundary layer was ignored. The reaction mechanism included the adsorption and desorption of six species, which were CH_4, O_2, CO, CO_2, H_2, and H_2O. Catalytic ignition was identified when the oxygen coverage on the catalyst surface showed a sudden drop. Their results supported the idea that CO and H_2 were formed directly from CH_4 oxidation. The reactor performance was mainly affected by the reaction temperature and the flow rate of the gas. It should be pointed out that their predictions of the yield of CO and H_2 did not match the experimental data well, especially when the gas inlet temperature was high.

Canu and Vecchi [33] simulated catalytic methane combustion in a monolith reactor using CFD. It was found that the gas-phase reaction had only a negligible effect on the methane conversion. They assumed that the flow was laminar and that the reaction happened on the catalytic surface. A global kinetic equation was used to calculate the rate of reaction. The composition change by the reaction was considered in the source term of the species and the energy equations. The reaction they studied was complete combustion because the volume ratio of O_2 to CH_4 was about 5.3.

Chaniotis and Poulika [34] compared the performance of two models, a surface perfectly-stirred-reactor model (1D) and a Navier-Stokes equation model (2D). Both models included a detailed surface reaction mechanism of CH_4 oxidation on rhodium in the prediction of reactor temperature, carbon soot formation, methane conversion, and hydrogen yield. This heterogeneous mechanism involved intermediate reaction steps (38 elementary surface reactions) and species (7 gas-phase and 12 site species). A single channel from a monolith structure was used as the modeling reactor. In general, the differences between the two models were less than 5–10%. They thought this was due to the use of the sophisticated reaction mechanism and the accurate prediction of the residence time for the stirred reactor model.

Hecht et al. [35] modeled methane steam reforming in the channel of an anode in a solid oxide fuel cell. Their model included an elementary heterogeneous reaction mechanism. It consisted of 42 irreversible reactions involving 6 gas-phase and 12 surface-adsorbed species. By comparing the products from kinetic simulations and products calculated from equilibrium, they found that the reactions did not reach equilibrium and were limited by kinetics.

Quiceno et al. [36] modeled catalytic partial oxidation of methane over a platinum gauze reactor. Their model integrated detailed gas-phase and surface reaction mechanisms into the numerical simulation of a three-dimensional flow field coupled with heat transport. Under their considered conditions, carbon monoxide, carbon dioxide and water were the main products at temperatures below 1270 K. Hydrogen can be formed above this temperature, but only in small amounts. They found that the surface reaction played a more important role than the gas-phase reaction because the main products were the same with and without the consideration of gas-phase chemistry. The homogeneous reaction mechanism consisted of 150 irreversible reactions among 30 species. The heterogeneous reaction mechanism included 36 irreversible reactions among 14 species. They compared their results with experimental data on CH_4 and O_2 conversion, and CO selectivity. Good agreement was obtained. They also considered the effects of residence time and pressure on the species distribution.

The reactor used by Hoang and Chan [19] for their ATR simulation had a diameter of 60 mm and a length of 350 mm. They multiplied the reaction rate by an effective factor coefficient to account for the rate decrease caused by the intra particle diffusion limitations. Their results showed that it took five minutes for the reforming process to reach steady state. The preferred time for start-up by the automobile manufacturers is 30–60 s [37].

Papadias et al. [20] developed a transient, 1D model for gasoline reforming in an adiabatic fuel processor. Their model consisted of a sub-model for the reactor and a sub-model for the kinetics. The reactor model included mass balance equations for the gas and catalyst phases, and energy balance equations for both gas and solid. They assumed that the reactions in ATR included exothermic total oxidation (Equation 2.13), endothermic steam reforming (Equation 2.14), and the equilibrium-limited WGS reaction (Equation 2.2).

These three non-elementary reactions were assumed to happen in a consecutive manner in their modeling work. The partial oxidation of the fuel is assumed to be the complete combustion of a portion of the fuel to CO_2 and H_2O. The direct partial oxidation of the fuel with oxygen to form CO and H_2 was ignored because the oxidation reactions are general very fast. The remainder of the fuel was consumed in the following steam reforming step.

The model was solved using a software package (FEMLAB 3.1), which is based on the finite element method to solve partial differential equations. Good agreement was found in the profiles of temperature, CO fraction, and H_2 fraction for the autothermal reforming mode with the use of this simple kinetic model. But some discrepancy was found in the initial fuel-rich stage of operation because of the formation of lower C_1–C_2 hydrocarbons in the experiment for both steady state and transient analyses.

Stutz and Poulikakos [38] numerically investigated the effect of thermal conductivity of the wall on methane reforming. The single channel of a monolith reactor with or without walls was used as the micro-reactor. It was found that the wall thermal conductivity had a significant effect on the wall surface temperature, which can directly affect the reforming reactions. Their results suggested that the reaction mechanism included an exothermic reaction with syngas as the products near the inlet, followed by the endothermic reforming reaction region. The mechanism they used was derived and validated by Schwiedernoch et al. [39]. The catalyst was assumed to be Rh.

It can be seen that methane is the most modeled fuel. Detailed reaction mechanisms have been developed for methane partial oxidation and steam reforming. It is expected that detailed mechanisms would be much more complicated for heavier hydrocarbons and difficult to validate. Modeling work for reforming processes using heavier hydrocarbons, such as those in gasoline or diesel, is limited.

2.6 Experimental Work

To provide hydrogen for fuel cell-based power systems, much research work has been focused on the reforming of liquid hydrocarbons that are commonly found in gasoline and diesel fuels experimentally using methods of SR, CPO, or ATR. Experimental studies confirmed that it is feasible to use gasoline or diesel reforming for hydrogen production [40-43]. The structure of the hydrocarbon affects the reforming efficiency. It was found that paraffins are relatively easier to reform than aromatics because they exhibit faster reaction rates [41].

CPO operates at much higher space velocities than SR and ATR [16]. For example, the gas hourly space velocity (GHSV) for the CPO of hydrocarbons is normally above 100,000 h^{-1} because of the rapid reaction rate. The GHSV for SR is typically around 5000-8000 h^{-1} on a wet feed basis. Therefore, the reactor size for CPO can be significantly reduced. The GHSV for ATR is in between that for CPO and SR. Usually, the total gross volume occupied by the monolith substrate is used to calculate the space velocity in the reactor.

The first generation of ATR catalyst developed by Engelhard Corporation [16] was based on a sequential reaction zone concept. The CPO only catalyst was followed by a separate SR only catalyst. The second generation of ATR catalyst was based on the overlapped reaction zone concept. The CPO washcoat layer was deposited directly on top of the SR washcoat layer in a single monolith.

Lindermeir et al. [44] studied a diesel-fuelled CPO reformer for SOFC-based auxiliary power unit (APU) systems (1 kWe). The system for the CPO reformer was less complicated than that for ATR. The fuel was a mixture of hydrocarbons, represented by a formula of $C_{16.2}H_{30.6}$. The composition of the catalyst was not given. Experiments were conducted using a reformer which included three zones, pre-catalyst, mixing, and main reaction. The product composition along the reactor length in the main reaction zone was determined. The measurement was obtained by gradually shortening the reactor length. The percentage of fuel converted reached 97% only after the 25 mm pre-catalyst zone. Temperature dropped from 940 to 780 ºC along the 150 mm reactor.

They also compared two CPO-based reformer designs to implement CPO [44]. The first one involved the integration of a heat exchanger with the CPO reformer to partially remove the heat released from the reactions. This type of design led to less durability and more soot deposition because of the high temperature at the front end of the catalyst. Its temperature can be more than 150 °C higher than the exit gas temperature. The second design involved the supply of fuel at two stages. First, a fraction of fuel reacts with the excess amount of air, and then the remaining fuel is fed into the hot off-gas. The efficiency for this approach was slightly less than that for the first approach with the heat exchanger. However, the two feed system is less complicated and the amount of the unconverted hydrocarbon measured was negligible. The researchers concluded that the second design is more suitable for fully-integrated, self-sustained applications.

Springmann et al. [45] designed a flat-bed reactor to kinetically study gasoline reforming at isothermal conditions. The actual temperature can be as high as 800 °C, and pressure can be 5 bar. Figure 2.3 shows a schematic diagram of the reactor. A mixture of steam, nitrogen, and the hydrocarbon being tested enters at the inlet. After the mixing section, there are four sampling ports. At the end is the outlet. The top and bottom surfaces are contacted by heating blocks which provide the energy required by the reactions. Catalyst is coated on the surface of a corrugated metal sheet, which is placed in the narrow space between the top and bottom surface. They found that the mole fraction of H_2 in the final product was increased by 8.5% with an increase of the reforming temperature from 625 to 675 °C for the steam reforming of iso-octane.

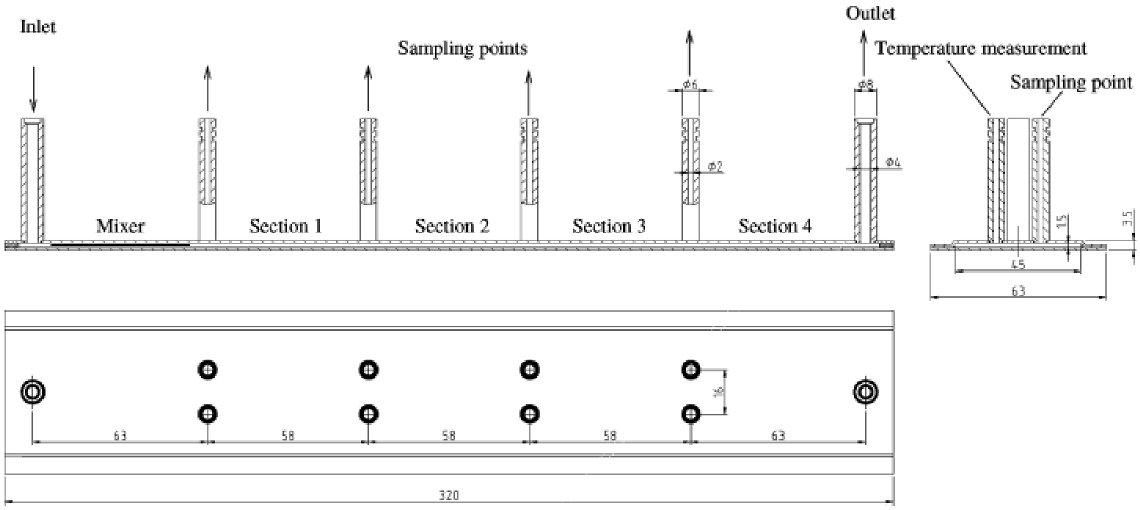

Figure 2.3. Schematic diagram of the flat-bed reactor used by Springmann et al. [45].

Liu et al. [31] studied the autothermal reforming of diesel using the experimental set-up shown in Figure 2.4. Their system includes a fuel delivery system, a catalytic reactor, and a reformate analysis system. The fuel delivery system ensured that the reactants are in the gas phase at the top of the catalytic reactor. Inside the catalytic reactor, catalytic reactions occur in the four monolith sections, which are connected by short ducts. The GHSV varied from 10,000 to 100,000 h^{-1}. The Reynolds number in the duct was about 2300 when the GHSV was 20,000 h^{-1}, but the Reynolds number was only about 40 in a single channel of the monolith section. This indicates that flow in the monolith is laminar. They found that the reforming efficiency increased with increases of the inlet oxygen-to-carbon ratio to values up to 0.42, after which it remained constant.

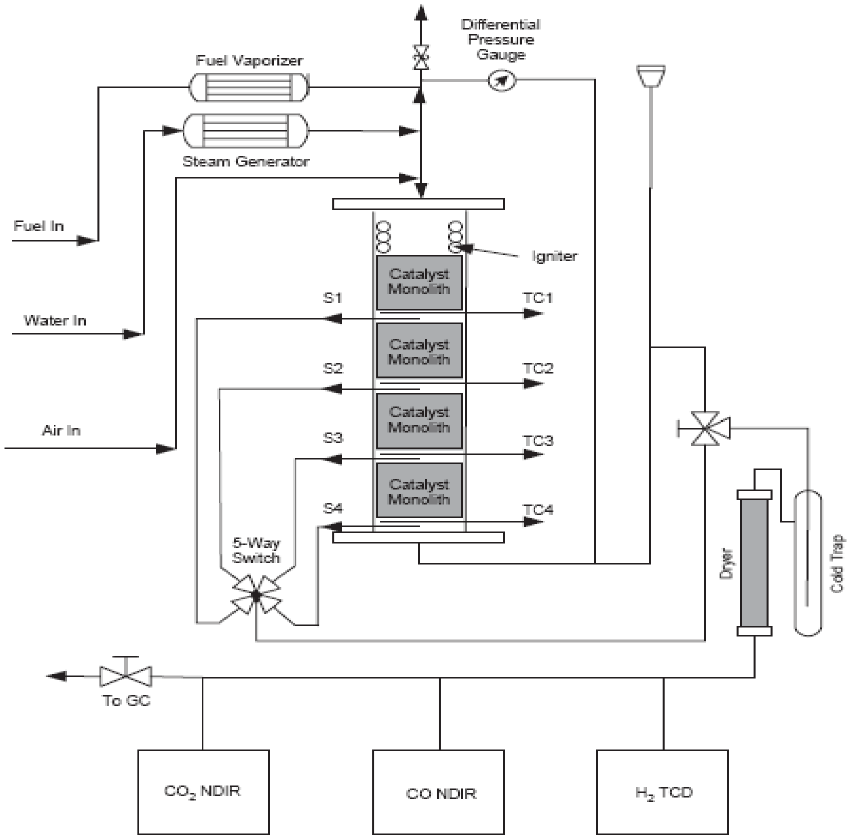

Figure 2.4. Schematic diagram of the ATR reactor used by Liu et al. [31].

CHAPTER 3: NUMERICAL MODEL

CFD-based numerical models can be used to study the scale-up and design of catalytic reactors. Two models were developed in this work, one for steam reforming using iso-octane (a surrogate for gasoline) and one for autothermal reforming using n-hexadecane (a surrogate for diesel fuel). Two different fuels were used in order to compare the simulation results with the available experimental data in the literature. In general, a CFD model for a fuel reformer includes two sub-models, one for the reactor and one for the reaction chemistry. The reactor model consists of the conservation equations of mass, momentum, energy, and species. The reaction chemistry model includes a reaction mechanism and kinetics for each reaction. The reaction mechanism defines the reactions happening in the reforming process. The kinetics provides the reaction rate expressions for each reaction. The two models used for the simulations are described below.

3.1 Model of Steam Reforming

This section is mainly based on a paper by Shi et al. [46] and the FLUENT 6.3 Users' Guide [47].

3.1.1 Model of a Single Channel

3.1.1.1 Geometry and Mesh

The flat-bed reactor used by Springmann et al. [45] had multiple channels inside. It was assumed that each channel behaved the same. Therefore, a single channel was chosen to model steam reforming. Only half of a single channel was modeled because of symmetry. According to the surface-to-volume ratio of 2360 m^2/m^3 and the gas void fraction of 0.67 [45], the width and height of a single channel were 1.7308 mm and 1.2167 mm, respectively. The length of the reactor in the axial direction (z) was 0.2003 m. Because the length of each channel was much larger than its width or height, only part of the modeled geometry is shown in Figure 3.1. The vertical surface was the symmetry plane. Catalyst was supported on the horizontal (or bottom) surface and the curved surface. The curve was assumed to be in the shape of a parabola.

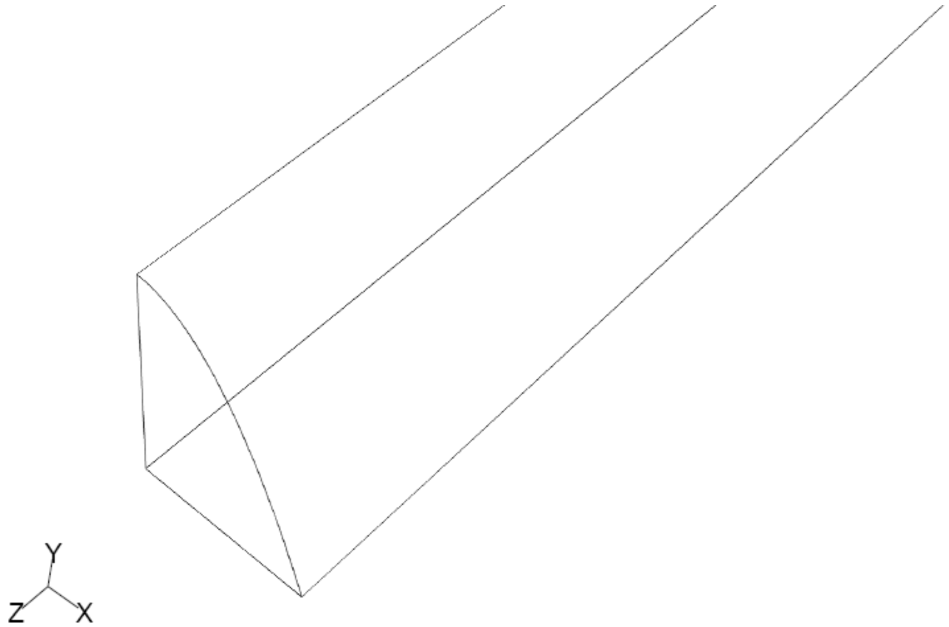

Figure 3.1. Schematic diagram of part of the modeled geometry.

Figure 3.2 shows a meshed surface in the x-y plane. It contained 496 elements. The element size near the corners was smaller than those in the middle. The total number of elements of the volume was appropriately 69,000. More meshes were given near the inlet. Mesh independent solutions were obtained.

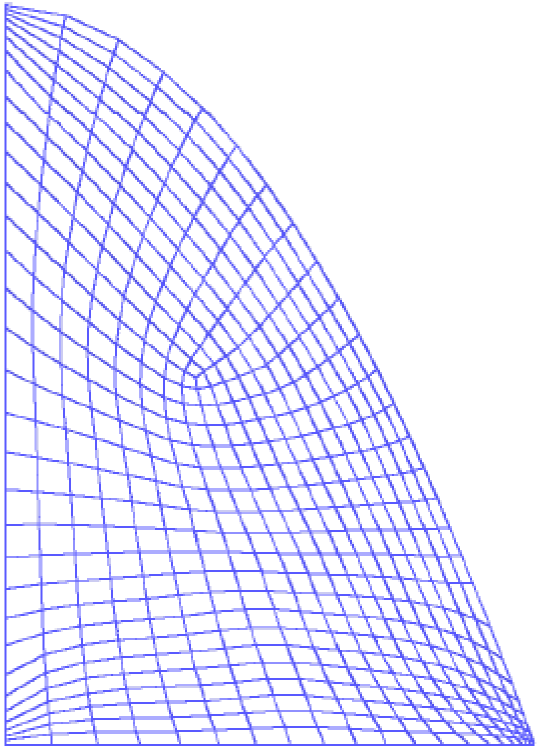

Figure 3.2. A meshed surface in the x-y plane.

3.1.1.2 Conservation Equations

According to the tested conditions of Springmann et al. [45], gas flow in the reactor was steady, incompressible, and laminar. Equations for continuity, momentum, energy and species [46-47] were solved by FLUENT 6.3.26 with a user-defined function to calculate the reaction rates. These relationships are given in Equations (3.1)-(3.4), respectively.

$$\frac{\partial u_j}{\partial x_j} = 0 \tag{3.1}$$

$$\rho u_j \frac{\partial u_i}{\partial x_j} = -\frac{\partial p}{\partial x_i} + \frac{\partial \tau_{ij}}{\partial x_j} + \rho g_i \tag{3.2}$$

$$\rho u_j \frac{\partial h}{\partial x_j} = \frac{\partial}{\partial x_j}(k_{eff} \frac{\partial T}{\partial x_j} - \sum_{i=1}^{N} h_i J_{ij}) + u_j \frac{\partial p}{\partial x_j} + S_h \tag{3.3}$$

$$\rho u_j \frac{\partial Y_i}{\partial x_j} = -\frac{\partial J_{ij}}{\partial x_j} + R_i \tag{3.4}$$

where u is the gas velocity (m/s), ρ is the gas density (kg/m^3), p is the static pressure (Pa), τ_{ij} is the laminar stress tensor (Pa), ρg is the gravitational body force per unit volume (N/m^3). h, k_{eff} and T are the sensible energy (kJ/kg), effective thermal conductivity (W/mK) and temperature (K) of gas mixture, respectively. h_i is the sensible energy of species i (kJ/kg), J_{ij} is the diffusional flux of species i in the j direction (kg/m^2·s), which was assumed to include full multicomponent diffusion and thermal diffusion. N is the total number of gas species, S_h is the source of energy caused by chemical reaction (kW/m^3). Y_i is the local mass fraction of species i, R_i is the net rate of production of species i by chemical reaction (kg/m^3·s).

The laminar stress tensor (τ_{ij}) is given by

$$\tau_{ij} = \mu(\frac{\partial u_i}{\partial x_j} + \frac{\partial u_j}{\partial x_i} - \frac{2}{3}\frac{\partial u_l}{\partial x_l}\delta_{ij}) \tag{3.5}$$

where μ is the molecular viscosity (N·s/m^2).

The first two terms on the right-hand side of Equation (3.3) represent energy transfer due to conduction and species diffusion, respectively. Thermal energy created by viscous shear in the flow was ignored. The effective thermal conductivity equals the thermal conductivity of the fluid in the model of steam reforming. The sensible enthalpy, h (kJ/kg), for an ideal gas mixture is defined as

$$h = \sum_{i}^{N} Y_i h_i \tag{3.6}$$

and h_i is given as

$$h_i = \int_{T_{ref}}^{T} C_{p,i} dT \tag{3.7}$$

where $C_{p,i}$ is the specific heat of species *i* (kJ/kg·K), and T_{ref} is the reference temperature, 298.15 K in this study.

The energy source term, S_h (kW/m^3) is calculated by

$$S_h = -\sum_{i} \frac{h_i^0}{M_{w,i}} R_i \tag{3.8}$$

where h_i^0 is the enthalpy of formation of species *i* (kJ/mol), $M_{w,i}$ is the molecular weight of species *i* (kg/mol).

Because the molecular transport process is significant in the fuel reformer, the diffusional flux of species *i*, J_{ij}, is solved using the full multicomponent diffusion method which is based on the Maxwell-Stefan equation and is written as

$$J_{ij} = -\sum_{\substack{k=1 \\ k \neq i}}^{N} \rho D_{ik} \frac{\partial Y_k}{\partial x_j} - D_{T,i} \frac{1}{T} \frac{\partial T}{\partial x_j} \tag{3.9}$$

where $D_{T,i}$ is the thermal diffusion coefficient for species *i* in the mixture, and D_{ik} is defined as:

$$D_{ik} = [D] = [A]^{-1}[B] \tag{3.10}$$

$$A_{ii} = -\left(\frac{X_i}{d_{iN}} \frac{M_w}{M_{w,N}} + \sum_{\substack{k=1 \\ k \neq i}}^{N} \frac{X_k}{d_{ik}} \frac{M_w}{M_{w,i}}\right) \tag{3.11}$$

$$A_{ik} = X_i\left(\frac{1}{d_{ik}}\frac{M_w}{M_{w,k}} - \frac{1}{d_{iN}}\frac{M_w}{M_{w,N}}\right) \qquad (3.12)$$

$$B_{ii} = -\left(X_i\frac{M_w}{M_{w,N}} + (1 - X_i)\frac{M_w}{M_{w,i}}\right) \qquad (3.13)$$

$$B_{ik} = X_i\left(\frac{M_w}{M_{w,k}} - \frac{M_w}{M_{w,N}}\right) \qquad (3.14)$$

where [A], [B], and [D] are (N-1) x (N-1) matrices. X_i is the molar fraction of species *i*. M_w is the molecular weight of the mixture, $M_{w,N}$ is the molecular weight of species *N,* and d_{ik} is the binary mass diffusion coefficient for species *i* in species *k*.

The thermal diffusion coefficient is calculated by

$$D_{T,i} = -2.59x10^{-7}T^{0.659}\left[\frac{M_{w,i}^{0.511}X_i}{\sum_{i=1}^{N} M_{w,i}^{0.511}X_i} - Y_i\right]\left[\frac{\sum_{i=1}^{N} M_{w,i}^{0.511}X_i}{\sum_{i=1}^{N} M_{w,i}^{0.489}X_i}\right] \qquad (3.15)$$

3.1.1.3 Physical Properties

The binary mass-diffusion coefficient is calculated using the Chapman-Enskog formula [47]. It is based on the kinetic theory of gases.

$$d_{ik} = 0.00188\frac{\left[T^3\left(\frac{1}{M_{w,i}} + \frac{1}{M_{w,k}}\right)\right]^{0.5}}{p_{abs}\sigma_{ik}^2\Omega_D} \qquad (3.16)$$

where p_{abs} is the absolute pressure, σ_{ik} is the effective Lennard-Jones diameter for the collision, and Ω_D is the diffusion collision integral.

σ_{ik} for a binary mixture is calculated as

$$\sigma_{ik} = 0.5(\sigma_i + \sigma_k) \qquad (3.17)$$

Ω_D is calculated by

$$\Omega_D = f(T_D^*) = f(\frac{T}{(\varepsilon / k_B)_{ik}}) \tag{3.18}$$

where $(\varepsilon / k_B)_{ik}$ for the mixture is given by

$$(\varepsilon / k_B)_{ik} = \sqrt{(\varepsilon / k_B)_i (\varepsilon / k_B)_k} \tag{3.19}$$

where k_B is the Boltzmann constant.

Density of the gas mixture obeys the ideal gas law. It is calculated by

$$\rho = \frac{p_{op} M_w}{RT} \tag{3.20}$$

where p_{op} is the operating pressure (Pa).

It was assumed that thermal conductivity, viscosity, or specific heat of species *i* is a function of temperature. It is expressed as

$$\phi_i = \sum_{k=1}^{m} C_k T^{k-1} \tag{3.21}$$

where ϕ can be k, μ, or C_p. T has the units of Kelvin.

The thermal conductivity, viscosity, or specific heat of gas mixture is calculated by

$$\phi = \sum_{i=1}^{N} Y_i \phi_i \tag{3.22}$$

3.1.2 Model of the Reaction Chemistry

Solid and site species are not considered in the chemistry model because the amount of these species is usually very small. The r_{th} surface reaction at the wall involving only gas species can be written as follows:

$$\sum_{i=1}^{N} g_{i,r}^{'} G_i \leftrightarrow \sum_{i=1}^{N} g_{i,r}^{"} G_i \tag{3.23}$$

where G_i represents the gas-phase species. $g_{i,r}^{'}$ is the stoichiometric coefficient for each reactant species i, and $g_{i,r}^{"}$ is the stoichiometric coefficient for each product species i. A reaction mechanism involves a list of reactions. Equation (3.23) can be applied to all the reactions in the system. The coefficient for the species that are not involved in the reaction is zero.

The default reaction rate expression used by FLUENT is in the format of a power law [47]. If a reaction rate is not expressed in this format, a user-defined function (UDF) should be written to define the reaction rate using the macro of DEFINE_SR_RATE. The UDFs used in the models of steam reforming and autothermal reforming are given in Appendices A and B, respectively. The net molar rate of production or consumption of each species i, $\hat{R}_i$ (kmol/m^2·s), is given by

$$\hat{R}_i = \sum_{k=1}^{N_{rxn}} (g_{i,r}^{"} - g_{i,r}^{'}) r_k \qquad i = 1,2,3,\cdots,N \tag{3.24}$$

where N_{rxn} is the total number of reactions, and r_k is the reaction rate of the k_{th} reaction.

Because steam reforming was dominated by heterogeneous catalytic reactions, our model assumed that reactions only happened on the catalytic wall surface. Reactions in the gas phase were ignored because their effect on the total reaction rate was negligible [36]. The interaction between fluid and chemistry was laminar/finite rate [47].

The actual reaction mechanism during the reforming process is unknown. The currently available reaction mechanisms with details usually contain hundreds of reactions for dozens of species. To include all these reactions in the CFD simulations would take a significant amount of time. Sometimes their inclusion may not be practical. Therefore, a reduced or simplified reaction mechanism or a small set of reactions was included in the CFD simulations.

3.1.2.1 Reaction Mechanism for Steam Reforming

For the steam reforming of iso-octane (C_8H_{18}), six species including C_8H_{18}, H_2O, H_2, CO, CO_2 and N_2 were assumed in the simulations. Since the gases at the inlet only included C_8H_{18}, H_2O and N_2 in the experiments [45], the same species were assumed in the simulations. The inlet condition approximately represented those after partial oxidation. N_2 should be included because it was introduced before partial oxidation and not reacted during partial oxidation. Specifically, the global reactions to represent steam reforming of C_8H_{18} include three reactions and are given by Equations (3.25-3.27).

$$C_8H_{18} + 8H_2O \leftrightarrow 8CO + 17H_2 \tag{3.25}$$

$$CO + H_2O \leftrightarrow CO_2 + H_2 \tag{3.26}$$

$$C_8H_{18} + 16H_2O \leftrightarrow 8CO_2 + 25H_2 \tag{3.27}$$

These reactions were assumed to be reversible. The products of the reaction in Equation (3.25) are CO and H_2, while those of the reaction in Equation (3.27) are CO_2 and H_2. Equation (3.26) is the water gas shift reaction. To understand the effect of the reaction in Equation (3.27) on hydrogen production, two reaction mechanisms were assumed. One mechanism included two reactions, as shown in Equations (3.25-3.26), while the other included three reactions, as shown in Equations (3.25-3.27).

3.1.2.2 Reaction Rate Expressions for Steam Reforming

Little research has been carried out to investigate the reaction kinetics of the steam reforming of C_8H_{18}. Empirical data indicate that catalysts greatly affect the reaction kinetics. To solve this problem, one approach is to use the rate expressions derived from methane (CH_4) steam reforming to describe C_8H_{18} steam reforming [10]. The rate coefficients in the reaction rate expressions were adjusted accordingly. The CFD simulations need to have accurate kinetic data to give better predictions.

As mentioned in Chapter 2, the Numaguchi and Kikuchi model [23], called the NK model, assumed that there are two global reactions, including Equations (3.26) and (3.28). It can be seen that CO_2 is produced from CO through the WGS reaction. Xu and Froment [22] inferred that other pathways may be possible to form CO_2 directly. Therefore, the Xu and Froment model [22], called the XF model, assumed that there are three reactions, including Equations (3.26), (3.28)-(3.29).

$$CH_4 + H_2O \leftrightarrow CO + 3H_2 \tag{3.28}$$

$$CH_4 + 2H_2O \leftrightarrow CO_2 + 4H_2 \tag{3.29}$$

Xu and Froment [22] performed methane steam reforming at temperatures of 500-575 °C to study the intrinsic kinetics. In the experiments conducted by Numaguchi and Kikuchi [23], the reactor temperature varied in the range of 401-887 °C. The range of temperatures investigated by Springmann et al. [45] was closer to that by Numaguchi and Kikuchi [23]. Therefore, reaction rate expressions for the reactions represented by Equations (3.25)-(3.26) were based on the NK model with minor modifications. In addition, the XF model needs the input of mole fraction of H_2 at the beginning of the reaction, which is not suitable to on-board reformers. It can be inferred that the XF model predicts a higher reaction rate than the NK model at the beginning of the reaction because of the small mole fraction of H_2, which has been confirmed by the work of de Smet et al. [24].

The rate expressions for the reactions in Equations (3.25)-(3.27) are given by

$$r_1 = \frac{k_1 (P_{C_8H_{18}} - P_{H_2}^3 P_{CO} / P_{H_2O} K_{e1})}{P_{H_2O}^{0.6}} \qquad \text{(kmol } C_8H_{18} \text{ reacted/m}^2\cdot\text{s)} \qquad (3.30)$$

$$r_2 = k_2 (P_{CO} - P_{H_2} P_{CO_2} / P_{H_2O} K_{e2}) \qquad \text{(kmol CO reacted/m}^2\cdot\text{s)} \qquad (3.31)$$

$$r_3 = \frac{k_3 (P_{C_8H_{18}} - P_{H_2}^4 P_{CO2} / P_{H_2O}^2 K_{e3})}{P_{H_2O}^{0.3}} \qquad \text{(kmol } C_8H_{18} \text{ reacted/m}^2\cdot\text{s)} \qquad (3.32)$$

$$k_i = A_i \exp(-E_i / RT) \qquad (i = 1, 2, 3) \qquad (3.33)$$

where r_i is the reaction rate, P_j is the partial pressure of species j (j = C_8H_{18}, H_2O, H_2, CO and CO_2) and k_i is the reaction rate coefficient. E_i is the activation energy. Values for the activation energy were based on those provided by Xu and Froment [22]. A_i is the pre-exponential factor and its values were adjusted until the simulation results at isothermal conditions provided a good match for the experimental data of Springmann et al. [45]. The values of both A_i and E_i are given in Table 3.1. R is the universal gas constant. Equation (3.32) was formulated using the same rationale used in the formulation of Equation (3.30).

Table 3.1. Values of A_i and E_i (i = 1, 2, 3) used in the simulations of steam reforming

Reaction	**Pre-exponential factor (A_i)**	**Activation energy (E_i) (kJ/mol)**
Equation (3.25)	1.4×10^{11} ($kmol/m^2 \cdot s \cdot bar^{0.4}$)	240.1
Equation (3.26)	25 ($kmol/m^2 \cdot s \cdot bar$)	67.1
Equation (3.27)	1.0×10^{11} ($kmol/m^2 \cdot s \cdot bar^{0.7}$)	243.9

K_{e1} and K_{e3} are the modified equilibrium constant of the reactions in Equations (3.25) and (3.27), respectively. K_{e2} is the overall partial pressure equilibrium constant of the WGS reaction. K_{ei} (i = 1, 2, 3) changes with temperature and is given by

$$K_{e1} = 8.1 \times 10^{6} (T)^{3.03} \exp(\frac{-202.3 \quad kJ/mol}{RT}) \qquad (\text{bar}^2) \tag{3.34}$$

$$K_{e2} = 9.01 \times 10^{-6} (T)^{0.968} \exp(\frac{43.6 \quad kJ/mol}{RT}) \tag{3.35}$$

$$K_{e3} = 4.926 \times 10^{5} (T)^{2.85} \exp(\frac{-166.38 \quad kJ/mol}{RT}) \qquad (\text{bar}^2) \tag{3.36}$$

K_{e1} and K_{e2} were based on the equations given by Aparicio [48]. K_{e3} was modified from the equilibrium constant of the reaction in Equation (3.29).

3.1.3 Boundary Conditions

Boundary conditions should be defined before numerically solving the above model. The velocity at the wall was assumed to be zero. For the energy equation, an isothermal condition means that the temperature of the wall is kept at a constant value. The heat flux at the wall is then calculated by

$$q = h_f (T_w - T_f) \tag{3.37}$$

where T_w is the wall temperature (K), T_f is local fluid temperature (K), and h_f is fluid-side local heat transfer coefficient (W/K). In laminar flow, h_f is computed by

$$h_f = \frac{k_f (\frac{\partial T}{\partial n})_{wall}}{(T_w - T_f)} \tag{3.38}$$

where n is the local coordinate normal to the wall, and k_f is the local thermal conductivity of fluid (W/m·K).

The boundary condition for the species equation (Equation 3.4) was defined so that the mass flux from external mass transfer to the wall equaled the rate of reaction at the wall surface. Mathematically, this can be expressed as

$$\rho_{wall} D_i \frac{\partial Y_{i,wall}}{\partial n} = M_{w,i} \hat{R}_i \qquad i = 1,2,3,\cdots,N \tag{3.39}$$

The above equation was used to solve the mass fraction of species at the wall. The catalyst layer was assumed to be very thin. This indicates that any effect from the resistance of internal diffusion can be ignored. To obtain the volumetric reaction rate (kmol/m^3·s) used in the species equation, the reaction rate $\hat{R}_i$ (kmol/m^2·s) based on the surface of the catalyst was divided by the height of the first cell adjacent to the wall.

The under-relaxation factors for pressure, density, momentum, energy, and species were 0.1, 0.3, 0.2, 0.95 and 0.9, respectively. Large changes in temperature because of the reactions result in large changes in gas density. To ensure stability in the flow solution, small under-relaxation factors should be used for pressure, density and momentum [47].

3.2 Model of Autothermal Reforming

Autothermal reforming is a preferred method for transportation applications because it is a self-sustained process. In the model of steam reforming, a single channel was used because it was assumed that each channel behaved the same. To eliminate this assumption and include the solid support in the model, a whole reactor was modeled for the case of autothermal reforming. To validate the simulation results, the reactor used by Liu et al. [31] was chosen in this study.

3.2.1 Model of the Whole Reactor

3.2.1.1 Geometry and Mesh

As mentioned in Chapter 2, the reactor consists of four monolithic sections with empty space in between. The monolith section includes gas flow channels and solid walls. The number of cells per square inch is 600 [31]. It is not possible to numerically solve the model if the actual monolith structure is modeled because the number of elements is very large. One strategy is to assume the monolithic section is a porous media. Then each mesh element includes both void space and solid material. The percentage of volume for gas flow is represented by the porosity.

Figure 3.3 shows the modeled geometry. Only a quarter of the reactor was modeled due to symmetry. The radius was 19.05 mm, and the length was 143.92 mm. The horizontal surface was the symmetrical plane at $x = 0$ m and the vertical surface was the symmetrical plane at $y = 0$ m. The curved surface was the wall of the reactor. The green regions represented the monolith zones. The mesh of the modeled geometry is shown in Figure 3.4. The total number of elements was 14,196. More meshes were put near the entrance of the first and second monolith zones because of the rapid change in the reaction rates in these two areas.

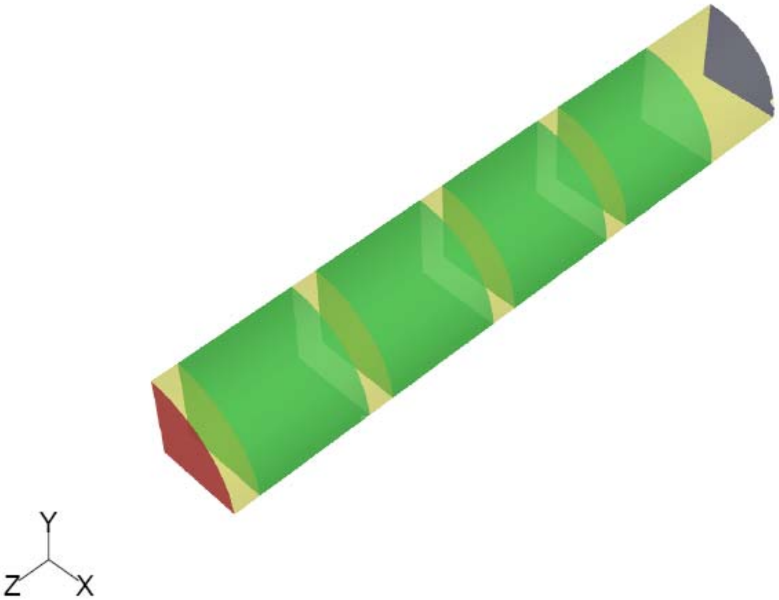

Figure 3.3. Geometry used in the model of the whole reactor.

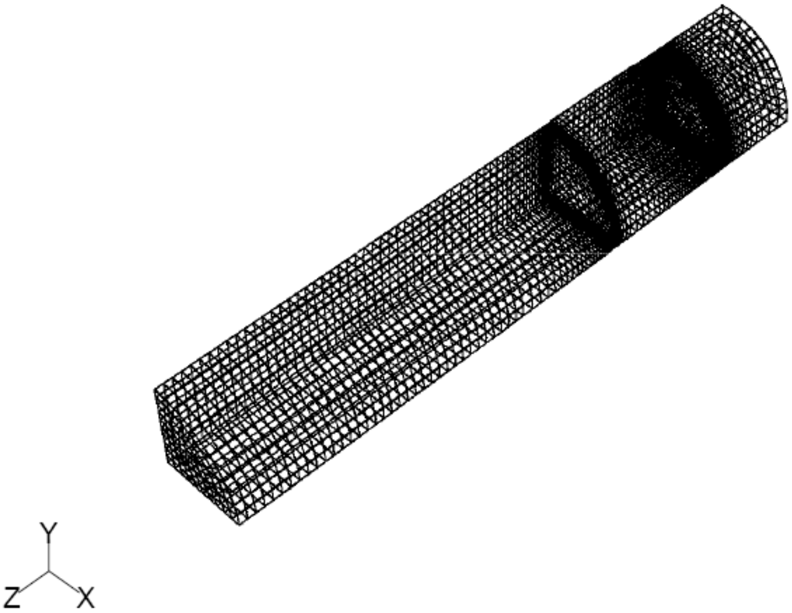

Figure 3.4. Mesh for the modeled geometry.

3.2.1.2 Conservation Equations

Most of the conservation equations used in the model of a single channel can be applied directly to the model of the whole reactor. This section only presents the difference between these two models, which is caused by the assumption of a porous media.

The presence of solid material in the monolith increased the resistance to fluid flow. Therefore, an additional term (S_u) was added in the momentum equation to account for this effect. The momentum equation for the monolith zones was written as

$$\rho u_j \frac{\partial u_i}{\partial x_j} = -\frac{\partial p}{\partial x_i} + \frac{\partial \tau_{ij}}{\partial x_j} + S_u \tag{3.40}$$

The gravitational body force was ignored because its effect was small. In general, the source term (S_u) included the viscous loss and the inertial loss. The inertial loss was ignored because the velocity was low. The viscous loss was calculated by

$$S_u = -\eta_{ij} \mu u_j \tag{3.41}$$

This loss was proportional to the velocity. The elements in the prescribed matrix η_{ij} were the resistance coefficients. The resistance coefficient in the axial direction was much smaller than that in each of the other two directions. This ensured that gases mainly flowed in the axial direction.

The effective thermal conductivity of the monolith zone used in the energy equation was given by

$$k_{eff} = \varepsilon k_f + (1-\varepsilon) k_s \tag{3.42}$$

where k_f and k_s are the thermal conductivity of fluid and solid medium, respectively. ε is the porosity of the monolith zone. A porosity of 0.64 was used for this model. This value for the porosity was calculated from the given dimensions.

3.2.2 Model of the Reaction Chemistry

Reaction was assumed to occur on the surface of solid walls. A surface-to-volume ratio is needed to model the monolith. A value of 3086 m^{-1} was used for this modeling.

3.2.2.1 Reaction Mechanism for Autothermal Reforming

Experimental data [31] showed that there were about 12% of CO_2 and 8% of CO in the product. Because the amount of CO_2 was larger than that of CO, complete combustion was assumed and the steam reforming reaction that resulted in CO_2 and H_2 was also included. The proposed global reactions for the autothermal reforming of $C_{16}H_{34}$ included

$$C_{16}H_{34} + 24.5O_2 \rightarrow 16CO_2 + 17H_2O \tag{3.43}$$

$$C_{16}H_{34} + 16H_2O \leftrightarrow 16CO + 33H_2 \tag{3.44}$$

$$CO + H_2O \leftrightarrow CO_2 + H_2 \tag{3.26}$$

$$C_{16}H_{34} + 32H_2O \leftrightarrow 16CO_2 + 49H_2 \tag{3.45}$$

The reaction in Equation (3.43) represents combustion. The reactions in Equations (3.44)-(3.45) represent steam reforming. The species at the inlet included $C_{16}H_{34}$, O_2, N_2, and H_2O. The amount of $C_{16}H_{34}$ that was cracked at high temperatures was ignored. Additional gas species including CO_2, CO, and H_2 were found at the outlet.

3.2.2.2 Reaction Rate Expressions for Autothermal Reforming

The reaction rate expressions for the above four reactions are given by

$$r_4 = \frac{k_4 P_{C_{16}H_{34}} P_{O_2}^{0.5}}{(1 + K_{C_{16}H_{34}} P_{C_{16}H_{34}} + K_{O_2} P_{O_2}^{0.5})^2} \qquad \text{(kmol } C_{16}H_{34} \text{ reacted/m}^2\cdot\text{s)} \tag{3.46}$$

$$r_5 = \frac{k_5 (P_{C_{16}H_{34}} - P_{H_2}^3 P_{CO} / P_{H_2O} K_{e5})}{P_{H_2O}^{0.6}} \qquad \text{(kmol } C_{16}H_{34} \text{ reacted/m}^2\cdot\text{s)} \tag{3.47}$$

$$r_2 = k_2 (P_{CO} - P_{H_2} P_{CO_2} / P_{H_2O} K_{e2}) \qquad \text{(kmol CO reacted/m}^2\cdot\text{s)} \tag{3.31}$$

$$r_6 = \frac{k_6 (P_{C_{16}H_{34}} - P_{H_2}^4 P_{CO_2} / P_{H_2O}^2 K_{e6})}{P_{H_2O}^{0.3}} \qquad \text{(kmol } C_{16}H_{34} \text{ reacted/m}^2\cdot\text{s)} \tag{3.48}$$

$$k_i = A_i \exp(-E_i / RT) \qquad (\text{i} = 2, 4, 5, 6) \tag{3.49}$$

where P_i is the partial pressure of species i (i = $C_{16}H_{34}$, H_2O, O_2, H_2, CO and CO_2). k_i represents the reaction rate coefficients. Equation (3.46) was based on the partial oxidation model of Ma et al. [26]. Equations (3.47)-(3.48) were similar to those used in the model of steam reforming. The values for A_i and E_i were adjusted until the simulation results matched the experimental data of Liu et al. [31]. The values of both A_i and E_i are given in Table 3.2.

Table 3.2. Values of A_i and E_i (i =2, 4, 5, 6) used in the simulations of autothermal reforming

Reaction	**Pre-exponential factor (A_i)**		**Activation energy (E_i) (kJ/mol)**
Equation (3.43)	8.11×10^6		86
Equation (3.44)	9.69×10^7	(kmol/m^2·s·bar$^{0.4}$)	240.1
Equation (3.26)	2.5	(kmol/m^2·s·bar)	54.5
Equation (3.45)	1.0×10^9	(kmol/m^2·s·bar$^{0.7}$)	243.9

K_{C16H34} and K_{O2} are the adsorption equilibrium constant of $C_{16}H_{34}$ and O_2, respectively. K_{e5} and K_{e6} are the modified equilibrium constants for Equations (3.44)-(3.45), respectively. These constants are given by

$$K_{C_{16}H_{34}} = 0.126\exp(\frac{-(-27.3) \quad kJ/mol}{RT}) \tag{3.50}$$

$$K_{O_2} = 7.87x10^{-7}\exp(\frac{-(-92.8) \quad kJ/mol}{RT}) \tag{3.51}$$

$$K_{e5} = K_{e1} = 8.1x10^{6}(T)^{3.03}\exp(\frac{-202.3 \quad kJ/mol}{RT}) \qquad (\text{bar}^2) \tag{3.52}$$

$$K_{e2} = 9.01x10^{-6}(T)^{0.968}\exp(\frac{43.6 \quad kJ/mol}{RT}) \tag{3.35}$$

$$K_{e6} = K_{e3} = 4.926x10^{5}(T)^{2.85}\exp(\frac{-166.38 \quad kJ/mol}{RT}) \quad (\text{bar}^2) \tag{3.53}$$

where T is the temperature (K). Values in Equations (3.50)-(3.51) were based on those for methane and oxygen used by Tiemersma et al. [49].

3.3 Equilibrium Analysis

An equilibrium analysis was performed using the ASPEN Plus [50] software program. This equilibrium analysis was based on the minimization of the Gibbs free energy. Since this analysis assumes that equilibrium has been reached, it gives the maximum possible yield at a given condition. For example, temperature and pressure of the reformer were required at isothermal conditions. Only pressure was required at adiabatic conditions because the amount of heat exchanged between the reformer and the surrounding was zero [51]. The difference between the amount of product from CFD simulations and that from the equilibrium analysis was used to evaluate the reformer performance. It is desirable if the amount of H_2 produced is close to that estimated at the equilibrium condition.

CHAPTER 4: CFD SIMULATION RESULTS OF STEAM REFORMING

This chapter presents the simulation results using the CFD model of steam reforming. The validation of the CFD model is given first, which is based on the paper of Shi et al. [46]. Then the effect of inlet H_2O/C molar ratio and the inlet velocity on the reformer performance are given.

4.1 Model Validation

Springmann et al. [45] performed steam reforming of iso-octane at two isothermal conditions, 625 and 675 °C, respectively. They found that the H_2 yield increased sharply in the first quarter of the reactor, and then increased slowly and became flat beyond the half length of the reactor. H_2, CO and CO_2 were the main products at both temperatures. A small amount of C_8H_{18} can be found at the reactor outlet when the temperature was 625 °C but not 675 °C.

The first part of model validation compares the CFD simulation results with the experimental data of Springmann et al. [45]. The second part compares these two sets of data with the results calculated at equilibrium conditions, which should define the maximum amount of hydrogen that can be produced.

4.1.1 Comparison with the Experimental Results

At isothermal conditions, the temperature of the catalytic wall at which reactions occur was held constant. The gases at the inlet represented the gas mixture after partial oxidation. The temperature of the gases at the inlet was assumed to be the same as the wall temperature. The flow rate through each channel was equal to the total flow rate divided by the number of channels. Temperature, pressure, and compositions distributed uniformly over the cross section at the inlet. Assuming that the molar flow rate was 0.2359 mol/hr, the pressure was 3 bar, the H_2O/C molar ratio was 3.2 and the N_2/C molar ratio was 4.33 at the inlet of the reactor, the simulated CFD results for H_2 mole fraction under the two reaction mechanisms which included the reactions in Equations 3.25-3.26 and the experimental data of Springmann et al. [45] are shown in Figure 4.1. The calculated mole fraction of H_2 was the mass-weighted average value among a cross sectional surface at a specified z location where z is the axial distance down the channel starting with $z = 0$ at the channel inlet and continuing to $z = L$ at the channel outlet. The percentage of difference is defined as the absolute difference between an experimental measurement and the corresponding simulation result divided by the experimental measurement, then multiplied by 100. Based on the mechanism of two reactions, the percentage of difference between each experimentally measured mole fraction of H_2 and the corresponding calculated CFD result was less than 17.7% at 625 °C and less than 15.6% at 675 °C. Therefore, the mole fractions of H_2 at both temperatures appear to be adequately predicted.

The slope of the mole fraction versus channel length curve for H_2 at 675 °C (Figure 4.1(b)) is steeper than the slope for the same curve plotted at 625 °C (Figure 4.1(a)) when z/L is less than 0.25. This indicates that the reaction rate was faster at 675 °C. The rapid change in the reaction rate near the entrance of the reactor can not be compared with experimental data because measured data [45] was not available.

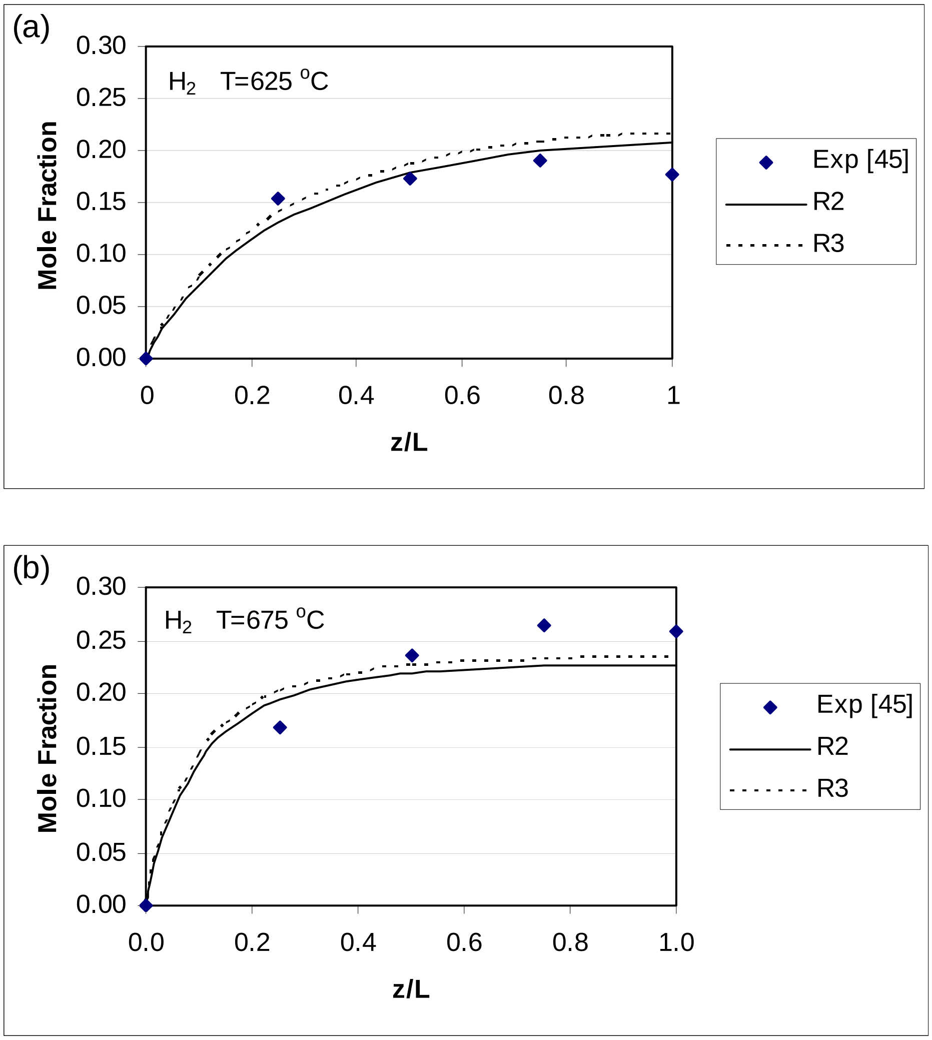

Figure 4.1. Mole fraction of H_2 (wet basis) as a function of the dimensionless length at (a) 625 °C and (b) 675 °C. Exp: experimental data [45]; R2: the mechanism of two reactions; R3: the mechanism of three reactions.

Figure 4.2 presents the mole fraction of H_2O as a function of the dimensionless length at the two temperatures. Except for the initial steeper slope of the curve than that found in the experiments [45], the CFD results predicted that more H_2O was consumed in the reactions at 625 °C, but this discrepancy disappeared at 675 °C. The large variations in the mole fractions of species occurred in the first quarter of the reactor, which is in agreement with the experimental measurements [45].

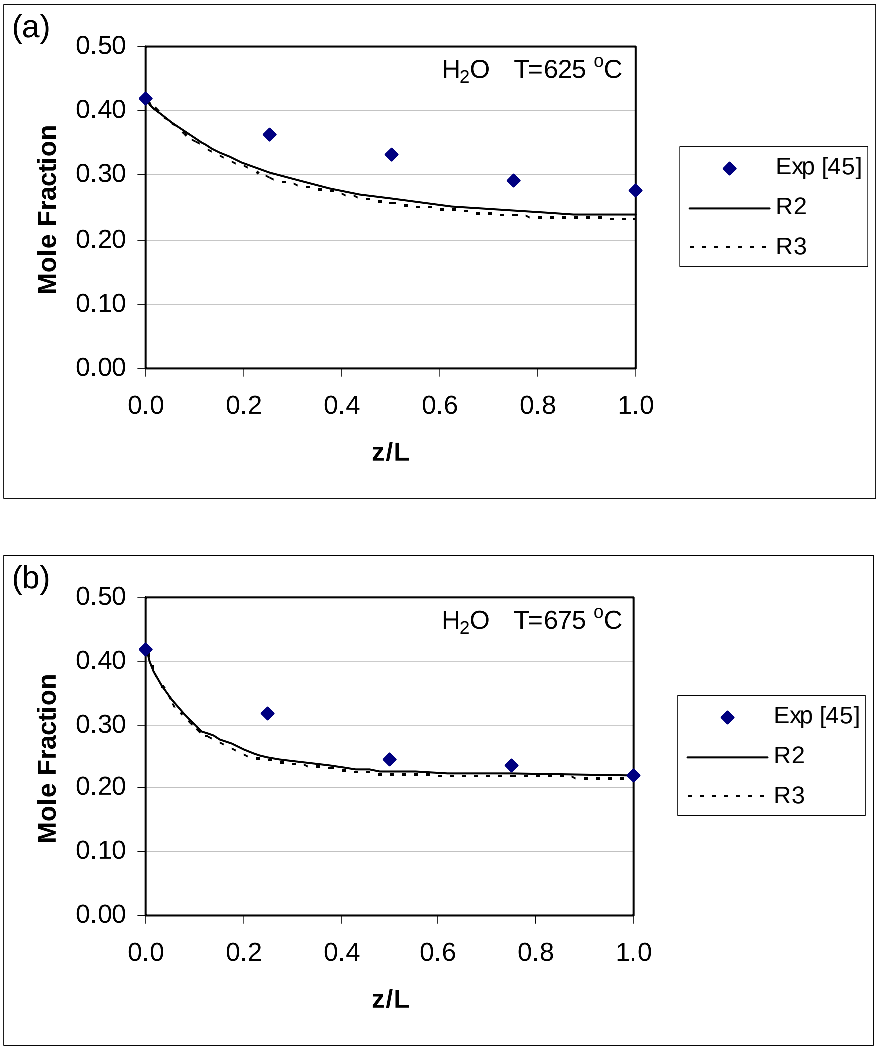

Figure 4.2. Mole fraction of H_2O (wet basis) as a function of the dimensionless length at (a) 625 °C and (b) 675 °C. Exp: experimental data [45]; R2: the mechanism of two reactions; R3: the mechanism of three reactions.

It can be seen from Figures 4.1 and 4.2 that the addition of the third reaction (Equation (3.27)) slightly increased the mole fraction of H_2 and reduced that of H_2O. Because the effect of the steam reforming reaction to form CO_2 and H_2 on the reforming process was small, the mechanism including two reactions was used in the following simulations. This is also supported by the measurements of Springmann et al. [45]. They found that H_2 and CO were the main products from the reaction between C_8H_{18} and H_2O

because the amount of CO_2 was small in the temperatures of 625-675 °C. This indicates that their catalyst was highly selective to H_2.

The modeling results in Figure 4.1 indicate that the reaction rate expressions in Equations (3.30)-(3.32) give good predictions of hydrogen yield from iso-octane reforming. These rate expressions initially developed for CH_4 reforming by Numaguchi and Kikuchi [23] in the format of Langmuir-Hinshelwood (LH), may be successfully used for the calculation of steam reforming of iso-octane with minor modifications. This suggests that methane steam reforming and iso-octane steam reforming may have similar rate-limiting steps. According to Aparicio [48], there may be multiple rate limiting steps during methane reforming. He also suggested that in the temperature range of 550-800 °C, the availability of surface oxygen, either O·S or OH·S, becomes one of the rate-limiting steps. Both species may be controlled by the surface adsorption of water and a dual site surface reaction between the adsorbed water and an active site. Much research about the fundamental reaction mechanism of iso-octane steam reforming is needed to identify the actual rate-limiting steps.

4.1.2 Comparison with the Results at Equilibrium

The amount of products at the equilibrium conditions from iso-octane steam reforming was calculated by minimizing the Gibbs free energy. This approach predicted the maximum amount of H_2 that can be produced at a given inlet condition.

It was assumed that the inlet streams included C_8H_{18}, H_2O and N_2 and the outlet streams included C_8H_{18}, H_2O, H_2, CO, CO_2 and N_2. Figure 4.3 shows the mole fraction of species obtained by three methods which include the experimental measurement, CFD simulation and equilibrium analysis at 625 and 675 °C. Only the mole fractions at the end of the reactor measured by Springmann et al. [45] or calculated by the CFD method were compared with the results at equilibrium because the equilibrium analysis does not consider the effect of time. Figure 4.3(a) shows that the mole fraction of H_2 from the experiment [45] or the CFD prediction is lower than that calculated at equilibrium at 625 °C. This is reversed for the mole fraction of C_8H_{18} or H_2O. The CFD prediction overestimated the amount of CO and underestimated the amount of CO_2 in the products because of the simplified reaction mechanism and their small amounts. Further investigation is needed to improve the prediction on CO and CO_2. According to Figure 4.3, the mole fraction of H_2 is increased and that of H_2O or C_8H_{18} is decreased as a result of the increase in temperature. This indicates that surface reaction was the rate-limiting step from 625 to 675 °C. The H_2 mole fraction measured by Springmann et al. [45] and predicted by the CFD method at 675 °C were approximately 94.2% and 82.6% of the value at equilibrium, respectively.

The amount of H_2O or CO in the product gases for both experiments [45] and CFD predictions was relatively higher than that at equilibrium. This suggests that the WGS reaction did not reach equilibrium in the reactor channel, which may be due to its slow reaction rate at temperatures in the range of 625-675 °C and short residence time in the reactor channel.

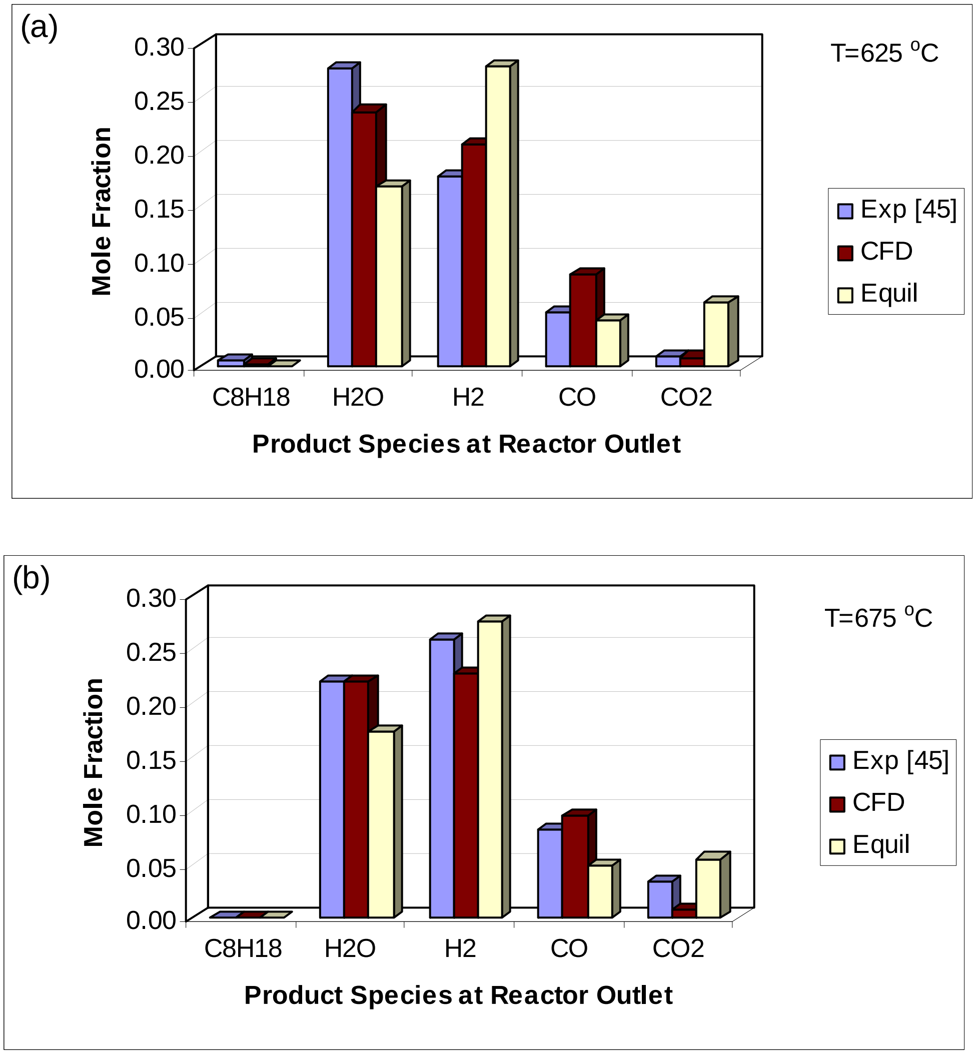

Figure 4.3. Comparison of the mole fractions of species (wet basis) using three methods at (a) 625 °C and (b) 675 °C. Exp: experimental measurement [45]; CFD: CFD simulation; Equil: equilibrium analysis.

4.2 Effect of Inlet H_2O/C Ratio on Reformer Performance

Solid carbon can be formed during steam reforming at low H_2O/C ratios. Higher H_2O/C ratios need more input of thermal energy, which is not readily available for transportation applications. In this work, the inlet H_2O/C molar ratio was varied from 2 to 4. C is the carbon molar content in the feed hydrocarbon. Table 4.1 gives the detailed values of gas compositions at the reactor channel inlet. The total molar flow rate of gases and the molar feed rate of C_8H_{18} were held constant, at values of 12.2691 mol/hr and 0.20034 mol/hr, respectively. It was assumed that the gas temperature at the inlet was 850 °C and the reactor pressure was 3 bar. The reactor was operated at adiabatic conditions.

Table 4.1. Gas compositions and values at the inlet

H_2O/C molar ratio		**2**	**3**	**4**
N_2/C molar ratio		5.5302	4.5302	3.5302
Mole fraction	C_8H_{18}	0.0163	0.0163	0.0163
	H_2O	0.2613	0.3919	0.5225
	N_2	0.7224	0.5918	0.4611
Mass fraction	C_8H_{18}	0.0695	0.0730	0.0770
	H_2O	0.1755	0.2768	0.3890
	N_2	0.7550	0.6502	0.5340
Mass flow rate in a half cell (kg/s)		1.7559e-6	1.6703e-6	1.5847e-6

4.2.1 Product Compositions and Reforming Efficiency

Figure 4.4 shows the mole fraction of gas species at the reactor outlet as a function of the inlet H_2O/C ratio. It can be seen from Figure 4.4(a) that the change in the mole fraction of H_2, CO, CO_2, and C_8H_{18} at the reactor outlet (wet basis) was negligible when the inlet H_2O/C ratio varied from 2 to 4. The mole fraction of H_2O in the products was 0.13, 0.24, and 0.35, corresponding to the inlet H_2O/C ratios of 2, 3, and 4, respectively. If water vapor was not included in the calculation (dry basis), the increase in the inlet H_2O/C ratio resulted in the increase in the mole fraction of H_2, CO, CO_2, and C_8H_{18}, see Figure 4.4(b). This is because the amount of water vapor in the product was high and it became higher at higher inlet H_2O/C ratios.

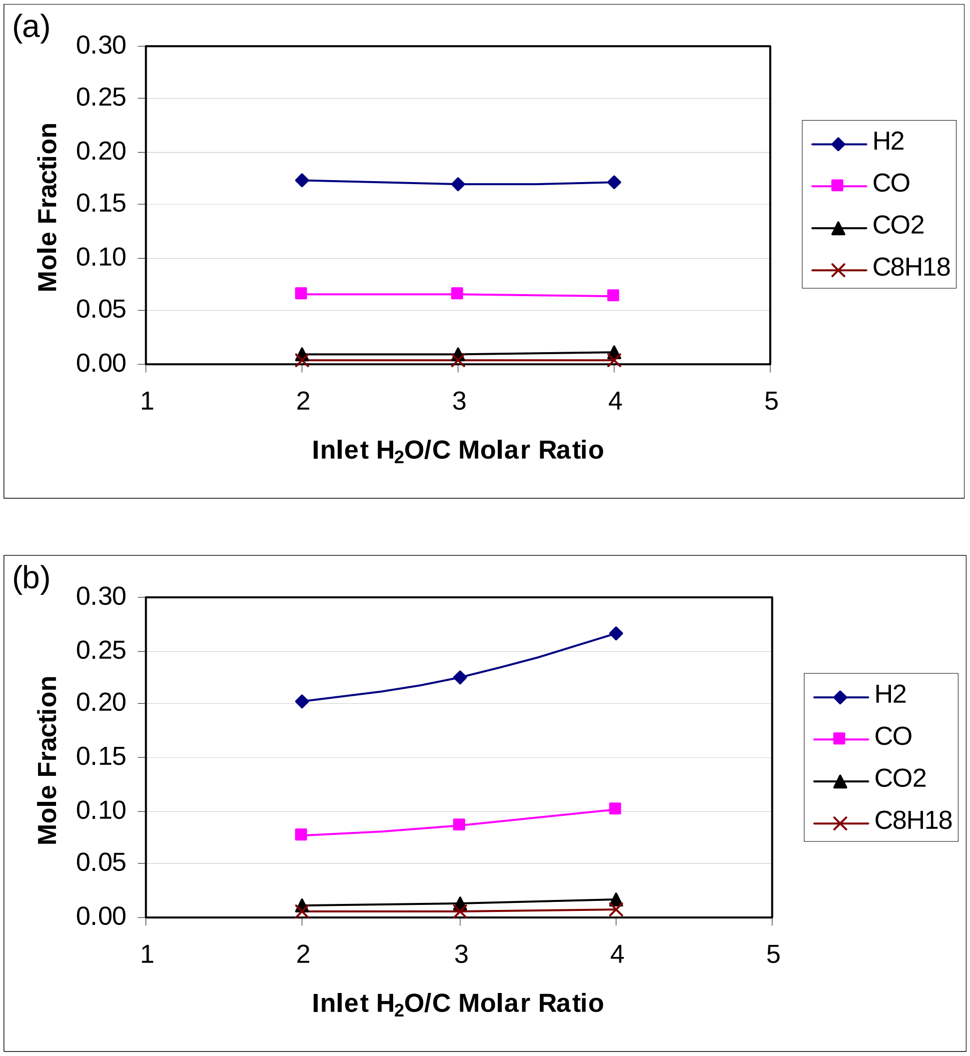

Figure 4.4. Mole fraction of gas species at the reactor outlet versus the inlet H_2O/C molar ratio, based on (a) wet basis and (b) dry basis.

The reforming efficiency based on H_2 (η_{H2}) is calculated by

$$\eta_{H2} = \frac{\dot{m}_{H2} * LHV_{H2}}{\dot{m}_{fuel} * LHV_{fuel}} \tag{4.1}$$

where $\dot{m}_{H2}$ (kg/s) and $\dot{m}_{fuel}$ (kg/s) are the mass flow rates of H_2 at a given location and that of the fuel at the inlet, respectively. LHV_{H2} (kJ/kg) and LHV_{fuel} (kJ/kg) are the lower heating values of H_2 and fuel, respectively. The *LHVs* are 120950 kJ/kg for H_2 and 44424 kJ/kg for C_8H_{18} at 25 °C.

Figure 4.5 shows the variation of reforming efficiency based on H_2 along the dimensionless length of the reactor. At a fixed inlet H_2O/C ratio, the reforming efficiency increased in the axial direction. Most of the increase occurred when z/L was less than 0.2. The reforming efficiency at inlet $H_2O/C = 2$ was slightly higher than those at other inlet H_2O/C ratios because of a relatively faster reaction rate. However, the reforming efficiency at various inlet H_2O/C ratios was nearly the same at the end of the reactor. It was around 60%. This is in agreement with the change in the mole fraction of H_2 (wet basis), which can be ignored at different inlet H_2O/C ratios.

Figure 4.6 shows the temperature profile along the dimensionless length of the reactor. At a fixed inlet H_2O/C ratio, the temperature of the reactor dropped quickly when z/L was less than 0.1 because of the fast reaction rate near the entrance of the reactor. The high temperature gases at the inlet provided the thermal energy for the reaction between C_8H_{18} and H_2O. Beyond z/L = 0.1, the temperature profile became flat because the reaction rate was low when temperature was below 600 °C. The outlet temperature at inlet $H_2O/C = 3$ or 4 was about 8-12 °C higher than that at inlet $H_2O/C = 2$ because of the steam reforming reaction.

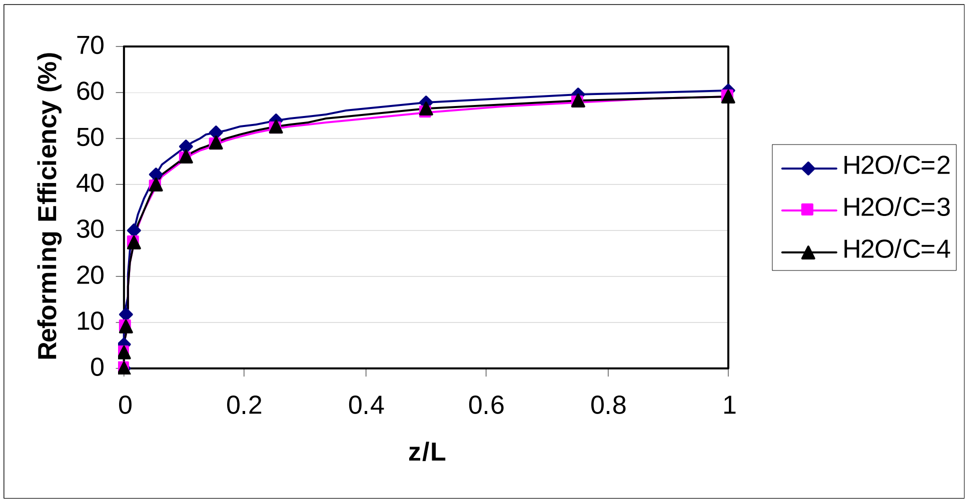

Figure 4.5. Reforming efficiency based on H_2 along the dimensionless length of the reactor at various inlet H_2O/C ratios.

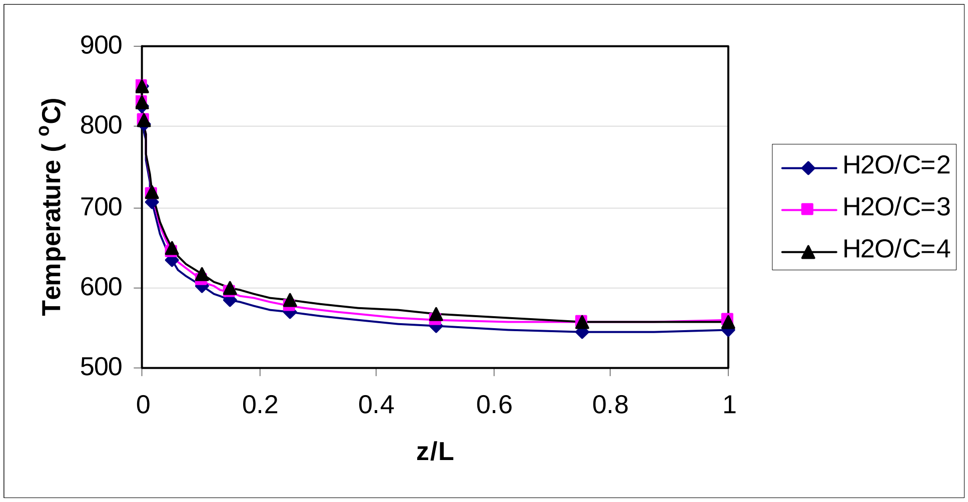

Figure 4.6. Temperature profile along the dimensionless length of the reactor at various inlet H_2O/C ratios.

The values shown in Figures 4.4-4.6 are the mass-weighted average values along the cross-sectional surfaces. To have a better view of H_2 distribution in a cross-sectional surface, contour plots of mole fraction of H_2 at two x-y surfaces are presented in Figure

4.7. The left contour is at z/L = 0.016 and the right one is at z/L = 0.1. Because reactions mainly occurred near the entrance of the reactor, there were five levels in the left contour plot. The mole fraction of H_2 was higher near the catalytic region due to the surface reaction. It gradually decreased toward the center of the reactor. At z/L = 0.1, the mole fraction of H_2 distributed uniformly across the x-y surface because of the convective mixing and slow reaction rate.

Similar changes were found in the contour plots of temperature (see Figure 4.8). At z/L = 0.016, lower temperature was near the catalytic region and higher temperature was in the middle of the reactor.

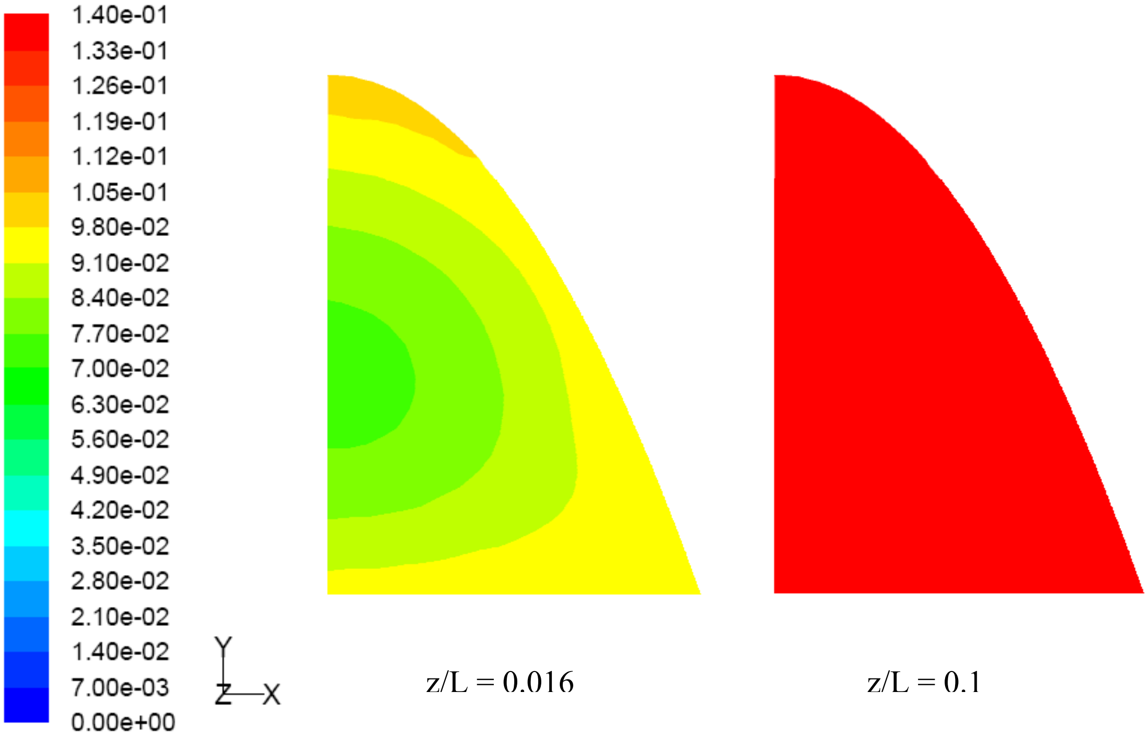

Figure 4.7. Contours of the mole fraction of H_2 on two x-y surfaces at inlet $H_2O/C = 3$. The scale on the left shows the mole fraction of H_2.

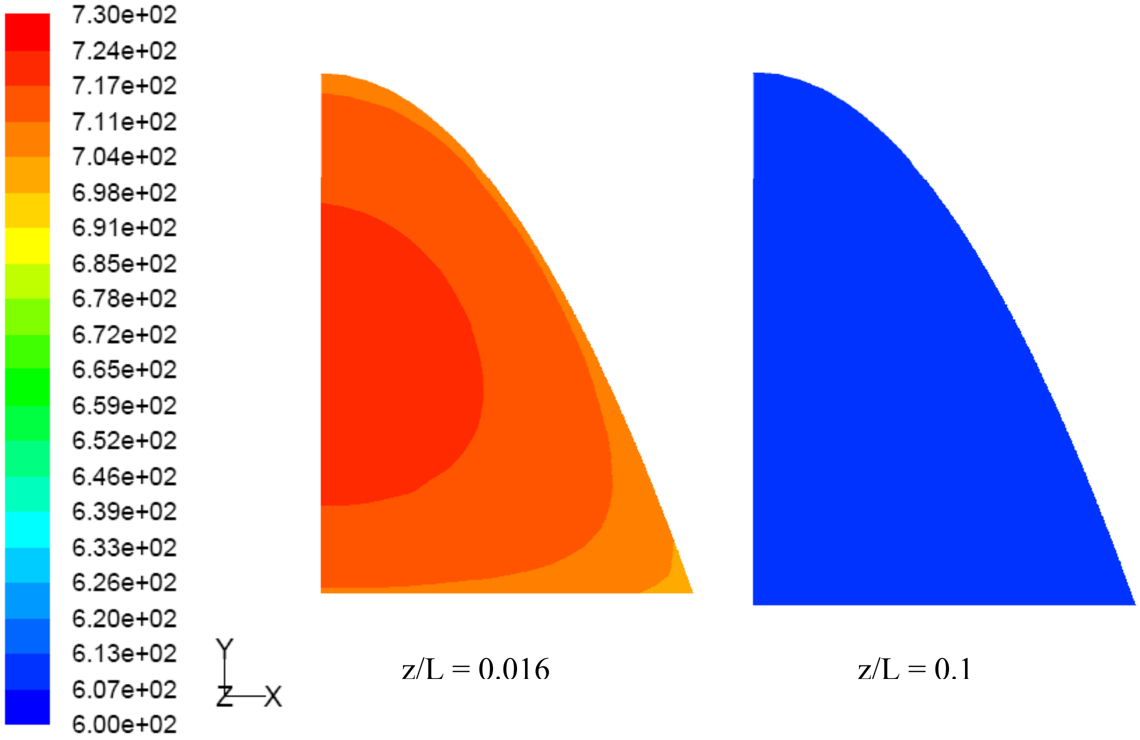

Figure 4.8. Contours of temperature on two x-y surfaces at inlet $H_2O/C = 3$. The scale on the left shows temperature (°C).

4.2.2 Comparison with the Equilibrium Results

For equilibrium analysis, the product only included H_2, CO, CO_2, C_8H_{18}, H_2O, and N_2. The results at the reactor outlet predicted by the CFD method were compared with those obtained by the equilibrium analysis and are shown in Figure 4.9. The mole fraction of H_2 at the equilibrium conditions only increased 10% due to the increase of inlet H_2O/C ratio. The mole fractions of H_2 predicted by CFD were about 58% of those calculated for equilibrium conditions. The difference is because of the reaction time, which is limited in CFD simulations. Figure 4.10 compares the mole fraction of gas species at the reactor outlet predicted by CFD simulation and equilibrium analysis at inlet $H_2O/C = 3$. It can be seen that the mole fraction of C_8H_{18}, H_2O, or CO predicted by CFD was higher than that estimated at the equilibrium conditions. This was reversed for the mole fraction of H_2 or CO_2. Similar variations were found at other inlet H_2O/C ratios.

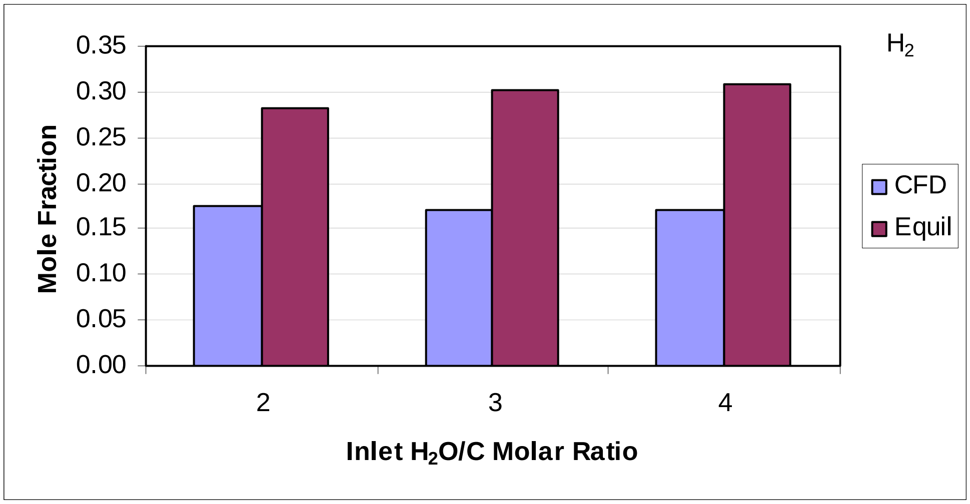

Figure 4.9. Comparison of mole fraction of H_2 predicted by the CFD method and equilibrium analysis at various inlet H_2O/C ratios (wet basis).

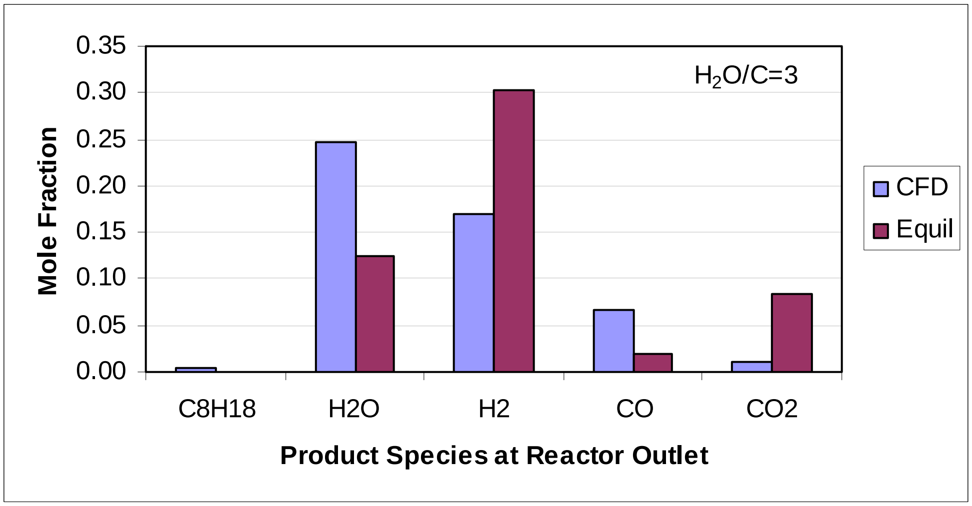

Figure 4.10. Comparison of mole fraction of gas species at the reactor outlet predicted by the CFD method and equilibrium analysis at inlet $H_2O/C = 3$ (wet basis).

4.3 Effect of Inlet Velocity on Reformer Performance

To produce more power from a reformer, one way is to increase the amount of reactants at the inlet. If the size of the reformer is fixed, the velocity of the reactants at the inlet is increased. This section presents results on the simulation of the influence of inlet velocity on the reformer performance.

The gas compositions studied at the inlet were the same as those listed in Table 4.1 under an inlet $H_2O/C = 3$. The total mass flow rate in a half cell was set at 1.6703e-6, 2.0879e-6, 2.5055e-6, 3.3406e-6, 4.1758e-6, and 5.0109e-6 kg/s, respectively. The corresponding inlet velocities were 2.9, 3.6, 4.4, 5.8, 7.3, and 8.7 m/s, respectively.

Figure 4.11 shows the mole fraction of gas species (wet basis) at the reactor outlet as a function of the inlet velocity. As the inlet velocity was increased from 2.9 to 8.7 m/s, the averaged mole fraction of H_2 at the outlet varied in the range of 0.163-0.170. The inlet velocity had negligible effect on the mole fraction of H_2. The mole fraction of CO was decreased by 14.5% as the inlet velocity increased. But the mole fraction of CO_2 or C_8H_{18} showed slight increase with increasing velocity. This is because less amount of C_8H_{18} was converted at higher velocities. Similar variations were obtained when the mole fractions were calculated on a dry basis.

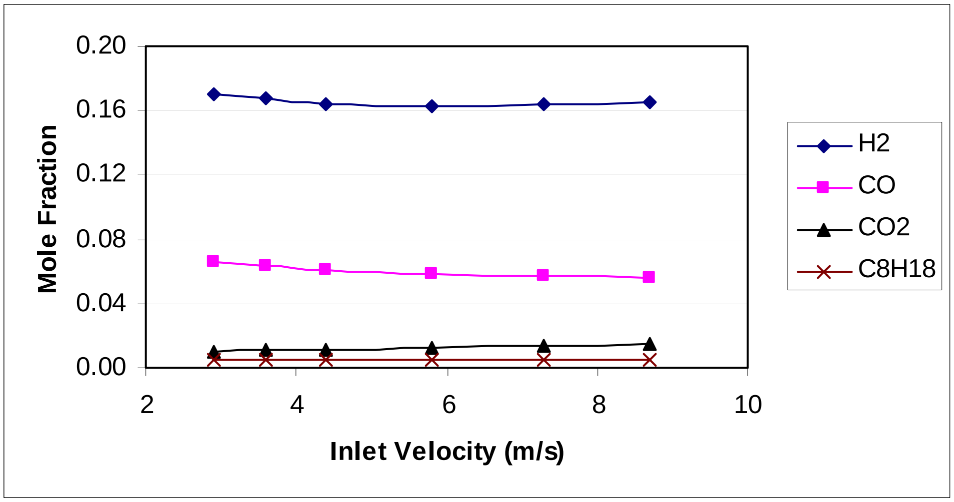

Figure 4.11. Mole fraction of gas species at the reactor outlet as a function of inlet velocity (wet basis).

The reforming efficiency based on H_2 along the reactor length at the three inlet velocities is given in Figure 4.12. The reforming efficiency for 2.9 m/s was higher than those for 5.8 or 8.7 m/s. The increase in velocity from 2.9 to 5.8 m/s resulted in a decrease in reforming efficiency. However, the increase in velocity from 5.8 to 8.7 m/s almost caused no change in the reforming efficiency. According to the reaction mechanism, H_2 can be produced from the steam reforming reaction (Equation 3.25) and WGS reaction (Equation 3.26). The steam reforming reaction accounted for the majority of H_2 produced. Since relatively more H_2 and CO were produced at 2.9 m/s, the difference in the reforming efficiency at the three inlet velocities was mainly due to the steam reforming reaction. Since the extent of steam reforming reaction was higher at the low velocity of 2.9 m/s, the reactor temperature should be lower than that at higher velocities. This is in agreement with the averaged temperature profile along the dimensionless length of the reactor, shown in Figure 4.13.

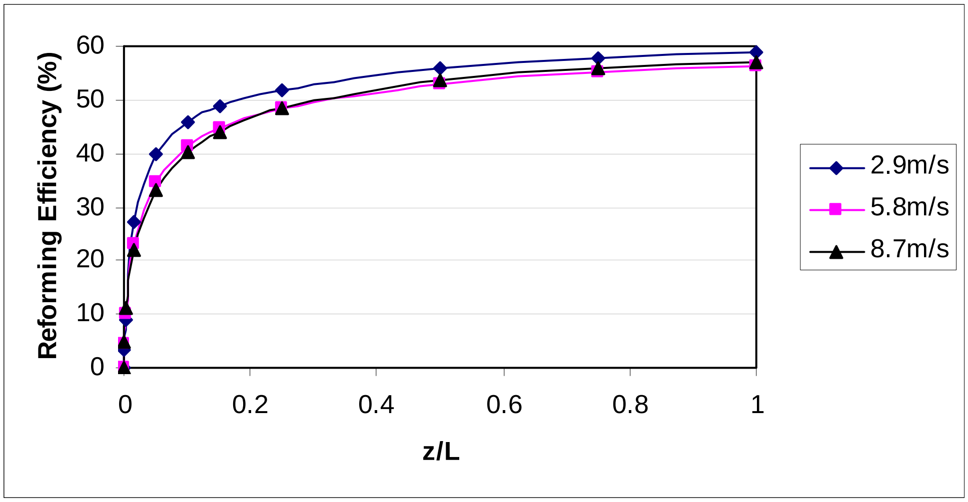

Figure 4.12. Reforming efficiency along the dimensionless length of the reactor at the three inlet velocities.

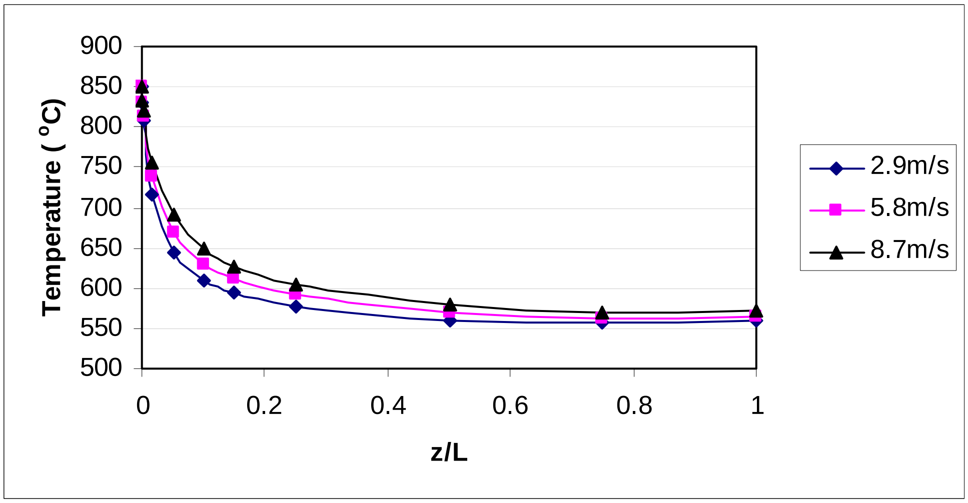

Figure 4.13. Averaged temperature along the dimensionless length of the reactor at the three inlet velocities.

Figure 4.14 shows the temperature profile on the symmetry plane (y-z surface) at the three inlet velocities. Only the first one tenth of the reactor is shown because temperature varied greatly in this region. The temperature contours at 2.9 m/s are relatively flatter than those at higher velocities. These contours are stretched more in the center as velocity increases. The relatively low temperatures near the top and bottom were because of the surface reaction. The center velocity was about 1.87 times of its corresponding inlet velocity. The increase in velocity reduced the residence time of reactants in the reactor.

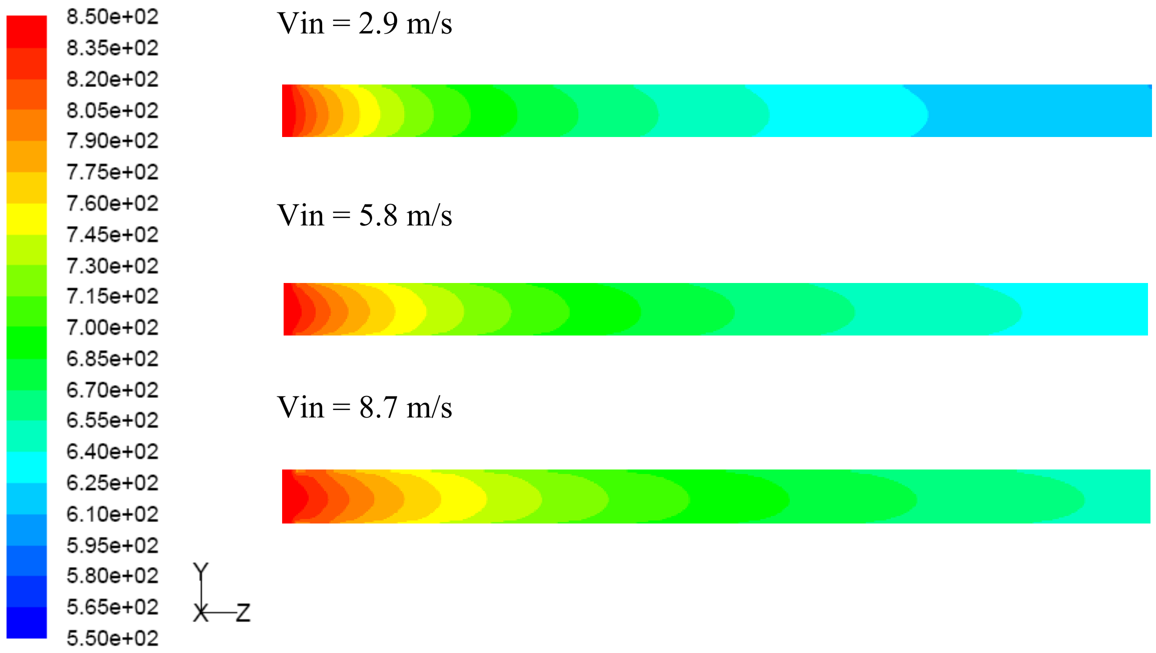

Figure 4.14. Contour plot of temperature on the symmetry plane (x = 0 m) at the three inlet velocities, the left scale shows temperature (°C).

CHAPTER 5: CFD SIMULATION RESULTS OF AUTOTHERMAL REFORMING

Diesel fuel has higher energy content per volume than gasoline. It is mainly used in heavy-duty trucks. There are several studies about reforming diesel to provide hydrogen for fuel cells [31, 40-42]. This chapter presents the model validation and simulation results using the CFD model of autothermal reforming. Parameters considered are the thermal conductivity of the solid catalyst support and power input.

5.1 Model Validation at an ATR Condition

Experimental data provided by Liu et al. [31] were used for model validation. They used n-hexadecane ($C_{16}H_{34}$) to represent diesel fuel in a kilowatt-scale catalytic monolith reactor. A schematic diagram of the reactor is shown in Figure 5.1, with the values of z and z/L on the right. The four areas filled with lines represent the four monolith zones. The reactor was kept at adiabatic conditions. The fuel and water were preheated to a gas (or vapor) phase before entering into the reactor. Data such as temperature and gas composition were measured at the end of each monolith zone.

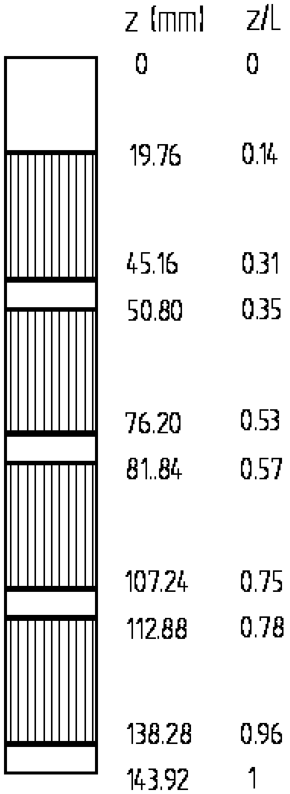

Figure 5.1. Schematic diagram of the monolith reactor with dimensions.

5.1.1 Comparison with Experimental Data

The experiment was performed at an inlet H_2O/C molar ratio of 2, an inlet O_2/C molar ratio of 0.37, and a power input of 5.7 kW [31]. Gas compositions at the inlet of the reactor are given in Table 5.1. Assuming the LHV of $C_{16}H_{34}$ was 10036.545 kJ/mol, the molar feed rate of $C_{16}H_{34}$ was 2.0445 mol/hr. The mass flow rate in a quarter of the reactor was 2.2944e-4 kg/s. It was also assumed that the inlet gas temperature was 327 °C (600 K), the pressure was 2 bar, and the thermal conductivity was 2.76 W/mK for cordierite, the material of the monolith reactor [31, 38]. Heat flux at the wall was set to zero to represent the adiabatic condition.

Table 5.1. Gas compositions and values at the inlet under autothermal reforming

H_2O/C molar ratio		2
O_2/C molar ratio		0.37
N_2/C molar ratio		1.3912
Mole fraction	$C_{16}H_{34}$	0.0163
	H_2O	0.5231
	O_2	0.0968
	N_2	0.3638
Mass fraction	$C_{16}H_{34}$	0.1401
	H_2O	0.3568
	O_2	0.1172
	N_2	0.3858

Figure 5.2 compares the predicted mole fractions (dry basis) of H_2, CO_2, and CO along the dimensionless length of the reactor with the experimental data [31]. The first set of experimental data was measured at the end of the first monolith zone. According to the CFD analysis, the averaged mole fraction of H_2, CO, and CO_2 increased rapidly in the first monolith zone ($z/L < 0.31$). Beyond that, the mole fraction of H_2 and CO increased slowly and that of CO_2 decreased slightly. The reforming efficiency based on H_2 was around 46.9% at the reactor exit. The mole fraction did not change in the duct which connected the monolith zones because of no surface reaction. This was reflected by the small flat portions in the curve. The measured data points distribute closely around the

curves of predicted mole fraction for the three species except those at z/L = 0.31 for H_2 and CO_2. The percentage of difference between each experimental measurement and the corresponding CFD prediction was below 16.8% for H_2, 17.3% for CO_2, and 16.0% for CO. Therefore, the simulated results matched the experimental data adequately for engineering design purposes.

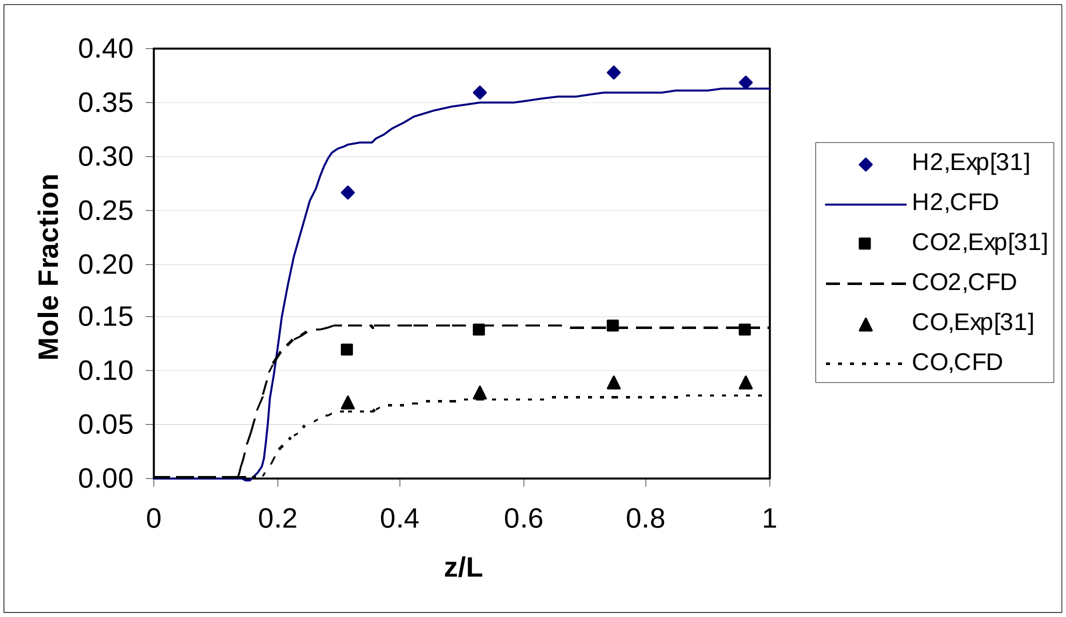

Figure 5.2. Averaged mole fractions (dry basis) of H_2, CO_2, and CO along the dimensionless length of the reactor.

Figure 5.3 shows the comparison between the predicted temperature along the dimensionless length of the reactor and the measured data. According to the CFD results, temperature reached its maximum value in the first half of the monolithic zone, and then decreased gradually. The sharp increase in temperature was caused by the combustion reaction. The subsequent temperature decrease was because of the endothermic steam reforming reactions. The simulated temperature was slightly higher than the measured data. But the percentage of difference was less than 11.6%. This indicates that the temperature profile was also satisfactorily predicted.

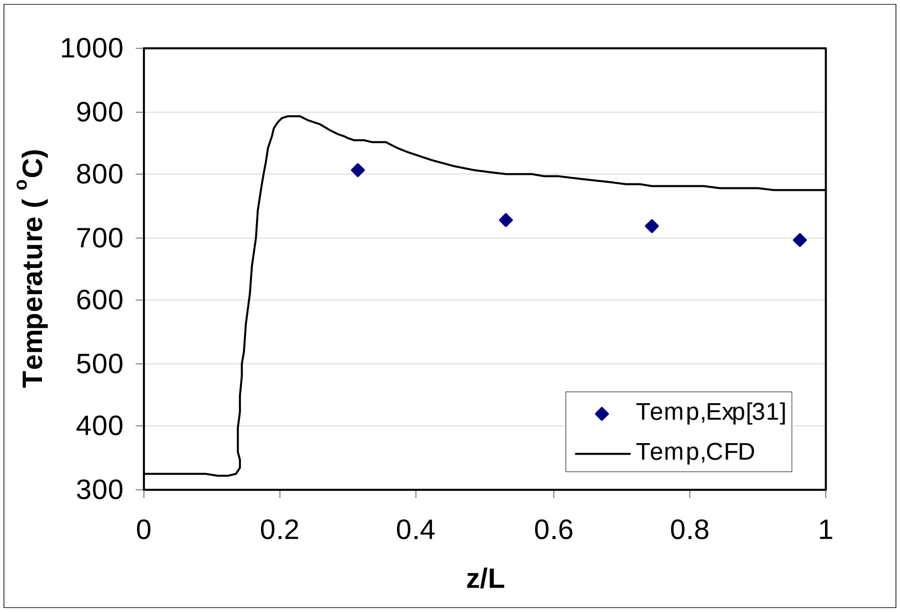

Figure 5.3. Averaged temperature profile along the dimensionless length of the reactor.

5.1.2 Comparison with the Equilibrium Results

In the equilibrium analysis, products only included H_2, CO, CO_2, $C_{16}H_{34}$, H_2O, O_2, and N_2. Figure 5.4 shows the mole fraction of H_2, CO_2, and CO obtained from the equilibrium analysis, CFD simulation, and experimental measurement. The mole fraction of H_2 predicted by CFD or measured by experiment [31] was less than the equilibrium value. They gave values that were about 80.3% and 81.7% of the predicted equilibrium values, respectively. One reason for this discrepancy may be that fuel was completely converted at the equilibrium condition. But only 72% of fuel was reformed in the reactor in the CFD simulation. The mole fractions of CO_2 and CO predicted by CFD modeling or measured experimentally were close to those calculated at the equilibrium condition.

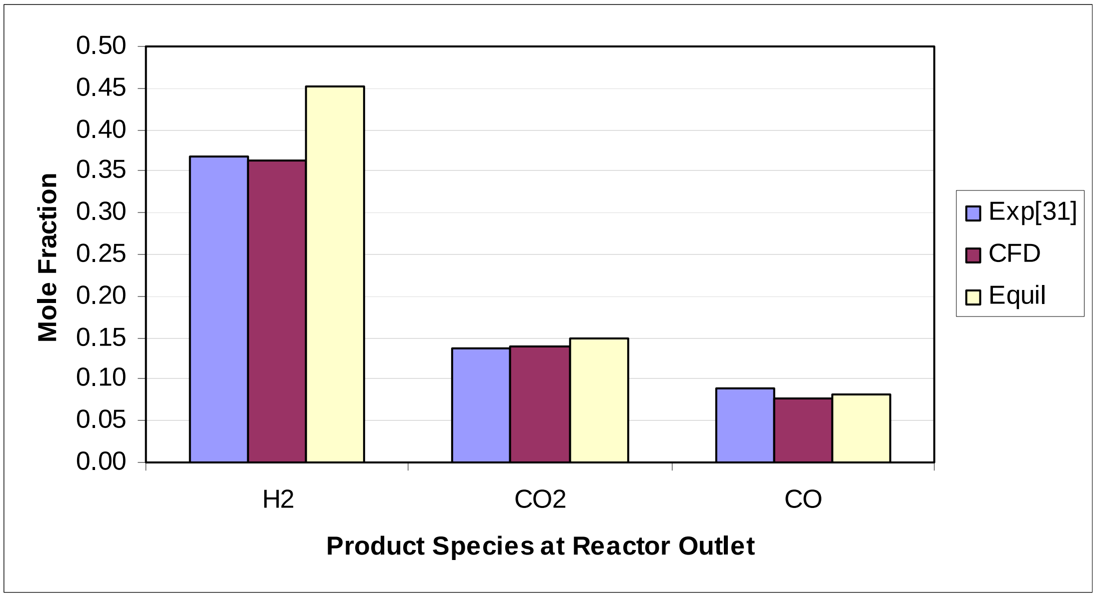

Figure 5.4. Comparison of mole fractions of products (dry basis) using three methods of experiment (Exp), CFD, and equilibrium (Equil).

5.2 Effect of Thermal Conductivity on Autothermal Reforming

Stutz et al. [38] found that the thermal conductivity of the catalyst support can affect the temperature profile along the length of the reactor by modeling a single channel of monolith with its wall. It is unclear how thermal conductivity affects the performance of the whole monolith reactor. This section presents the results of autothermal reforming by varying the thermal conductivity of catalyst support.

For the conservation equation of energy, thermal conductivity in the porous region was a combination of catalyst support (solid material) and gases, weighted by the porosity. Each computational grid contained both solid material and empty space for gas flow. The surface between the solid material and gases was not clearly separated. Both solid material and gases were affected by the heat released from the reaction.

The thermal conductivity was varied from 2.76 to 202.4 W/m·K, which represented the ceramic material and metallic material as the catalyst support, respectively. Other conditions were kept the same as those listed in Table 5.1. Figure 5.5 shows the contour of temperature on the symmetry surface of $x = 0$ m at four thermal conductivities. Similar changes was found on the symmetry surface of $y = 0$ m. The symmetry surfaces can be seen in Figure 3.3. Reactants flowed from the left to the right. Temperature changed rapidly from the inlet temperature to its maximum temperature near the entrance of the first monolith zone. The axial length for this change was shortened with the increase in thermal conductivity. This is because higher thermal conductivity conducted the heat released from the reaction faster. Corresponding to the thermal conductivity of 2.76, 27.6, 55.2, and 202.4 W/m·K, the maximum temperature in the reactor was 895.8, 882.3, 875.9, and 866.6 °C, respectively. It decreased about 30 °C as thermal conductivity increased by 73 times. Thermal conductivity did affect the temperature profile in the reactor. This is in agreement with the results of Stutz et al. [38], but the absolute temperature difference was small.

Figure 5.6 shows the averaged mole fractions of H_2, CO, and CO_2 at the end of the reactor versus thermal conductivity. With increasing thermal conductivity, the mole fraction of H_2 and CO was decreased by 0.9% and 2.0%, respectively, and that of CO_2 was increased by 0.5%. In comparison with the large change in thermal conductivity, this effect on the mole fraction of products was negligible.

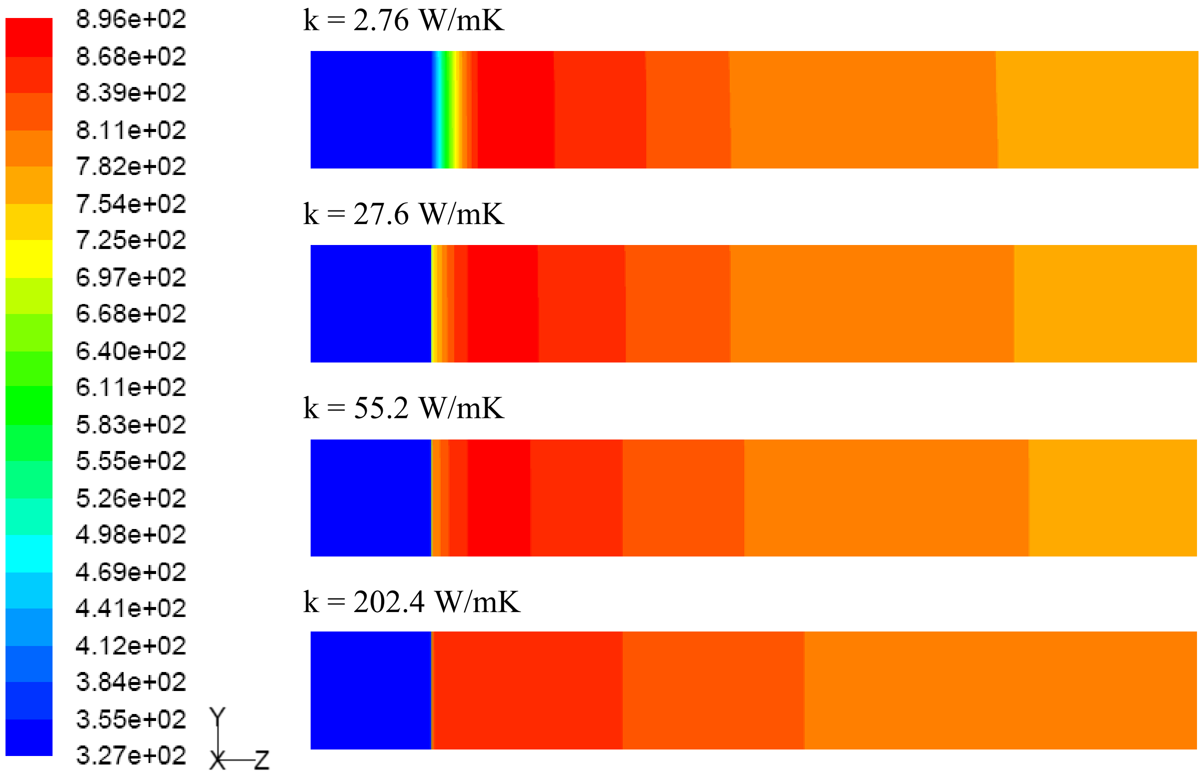

Figure 5.5. Temperature distribution on the symmetry surface of x = 0 m, temperature scale (°C) is shown on the left.

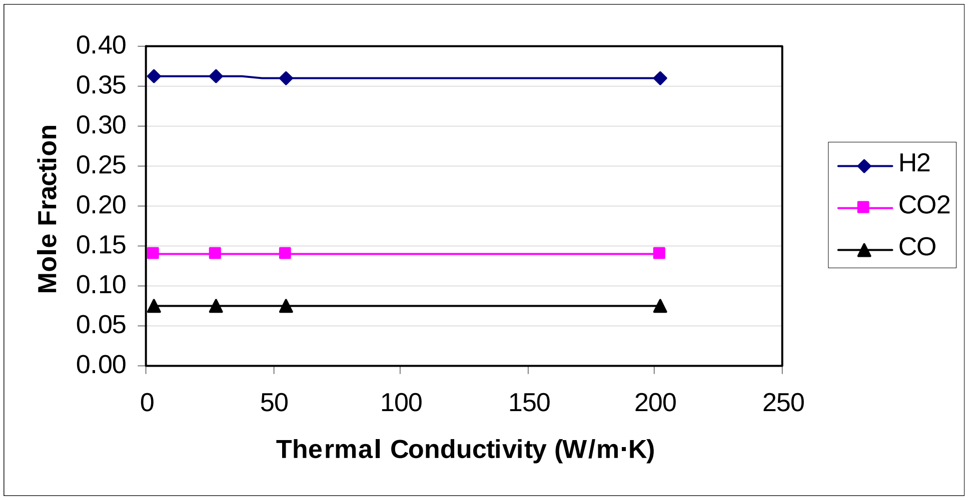

Figure 5.6. Averaged mole fractions (dry basis) of H_2, CO, and CO_2 at the end of the reactor as a function of thermal conductivity.

5.3 Effect of Power Input on Reformer Performance

5.3.1 Reforming Efficiency and Pressure Drop

The change of power input was directly caused by the variation in fuel feed rate. Other conditions were kept the same as those in Table 5.1. The tested conditions are given in Table 5.2. Table 5.2 gives the value of power input, fuel feed rate, inlet velocity, and mass flow rate in a quarter of the reactor. Figure 5.7 shows the reforming efficiency based on H_2 as a function of power input. As the power input increased from 1.7 kW to 8.4 kW, the reforming efficiency decreased from 50.9% to 45.0%, a reduction of 11.5%. Based on the assumed conditions, higher power input led to higher velocity in the reactor. Because the length of the reactor was constant, the residence time of reactants in the reactor decreased. This decrease in residence time resulted in a decrease in the amount of H_2 produced per unit of fuel fed and, subsequently, in a reduction in the reforming efficiency.

Table 5.2. Tested conditions at various power inputs

Power input (kW)	**1.7**	**2.8**	**5.7**	**8.4**
Fuel ($C_{16}H_{34}$) feed rate (mol/hr)	0.6098	1.0043	2.0445	3.013
Inlet velocity (m/s)	0.227	0.375	0.763	1.124
Mass flow rate in a quarter of the reactor (kg/s)	6.8434e-5	1.1271e-4	2.2944e-4	3.3813e-4

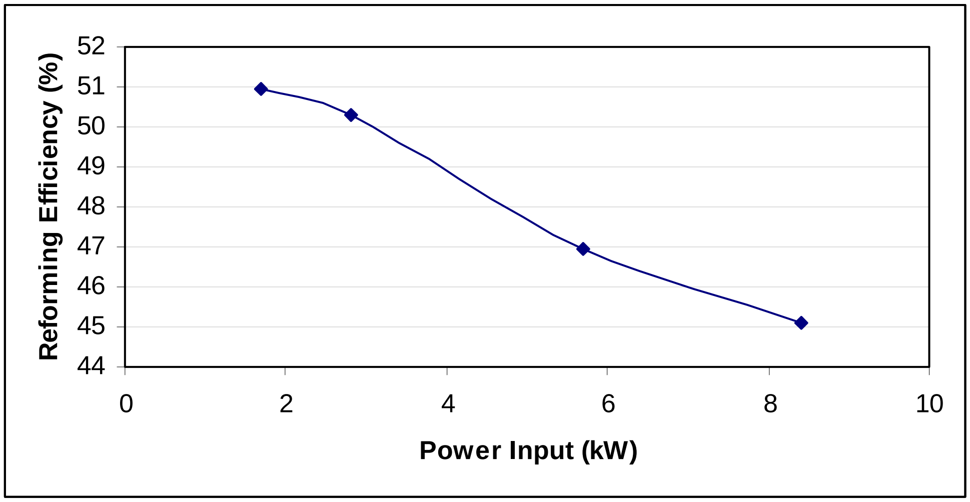

Figure 5.7. Reforming efficiency based on H_2 as a function of power input.

Figure 5.8 shows the area-weighted average mole fraction of H_2, CO, and CO_2 along the dimensionless length of the reactor. The curve of the mole fraction became less steep with increasing power input, especially in the first monolith zone. It can be seen from Figure 5.8(a) that about 86.7% of H_2 was produced by the end of the first monolith zone at 1.7 kW. In comparison, about 52.5% and 90.0% of H_2 was produced at the end of first and second monolith zone at 8.4 kW, respectively. To achieve similar mole fractions of H_2 in the product gas, the length of the reaction surface would need to be doubled when the power input changed from 1.7 to 8.4 kW.

The effect of power input or fuel feed rate on the mole fraction of CO was similar to that on the H_2 mole fraction. When the power input was increased from 1.7 to 8.4 kW, the mole fraction of CO at the outlet dropped from 0.091 to 0.072 (see Figure 5.8(b)), while that of CO_2 at the outlet was increased from 0.131 to 0.142 (see Figure 5.8(c)). Even at 8.4 kW, about 93% of CO_2 was produced in the first monolith zone. Power input affected the distribution of mole fraction of products in the reactor. The sharp change in

H_2, CO, and CO_2 at the beginning of the first monolith was because of combustion and steam reforming to form CO_2 and H_2. The subsequent slow increase in H_2 and CO was because of water gas shift reaction and steam reforming to form CO and H_2.

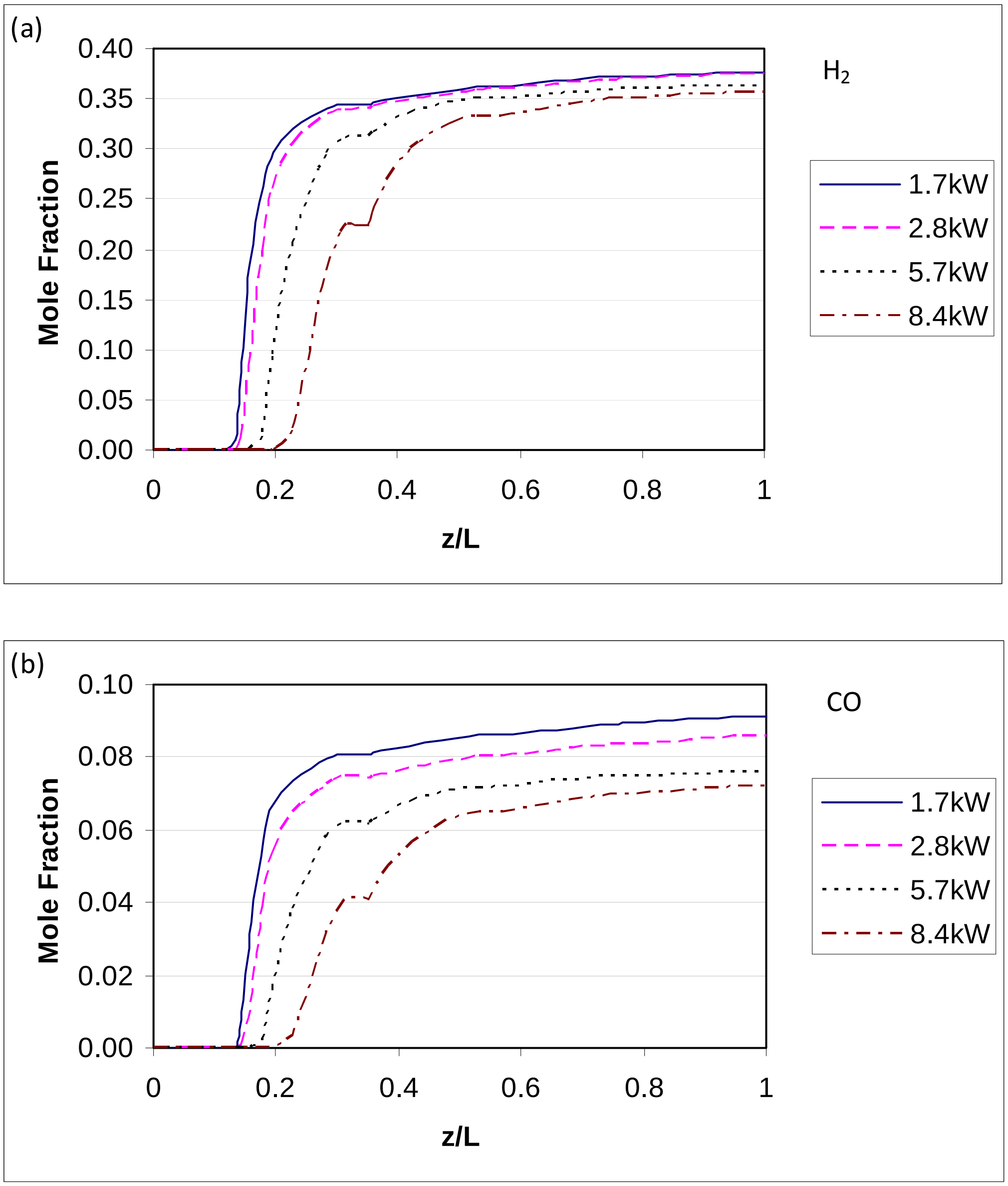

Figure 5.8. Averaged mole fractions of (a) H_2, (b) CO, and (c) CO_2 along the dimensionless length of the reactor at various power inputs.

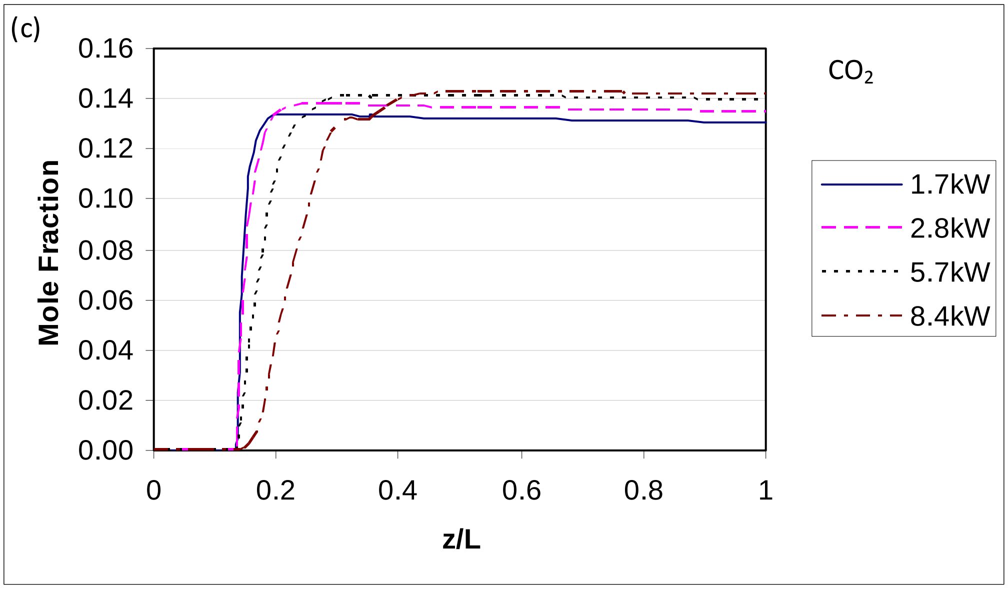

Figure 5.8(Continued). Averaged mole fractions of (a) H_2, (b) CO, and (c) CO_2 along the dimensionless length of the reactor at various power inputs.

Figure 5.9 shows the averaged temperature distribution along the dimensionless length of the reactor. As power input increased, the temperature profile shifted toward the reactor outlet and the location corresponding to the maximum temperature changed from z/L = 0.158 to 0.283. The shift in temperature profile was because of the change in the gas velocity.

Assuming that the viscous resistance coefficient was 7e+7 $1/m^2$ in the z direction and 7e+10 $1/m^2$ in the x or y direction, Figure 5.10 shows the pressure versus the axial position in the simulated reactor at various power inputs. The pressure drop over the reactor system was increased from 150 to 720 Pa when the power input was increased from 1.7 to 8.4 kW. Higher velocity resulted in higher pressure loss because it was assumed that the viscous loss was proportional to the velocity magnitude. The pressure drop was low in the simulated monolith reactor. It mainly dropped in the four monolithic zones because of the presence of the solid catalyst support. The pressure drop can be ignored in the duct between adjacent monolith zones.

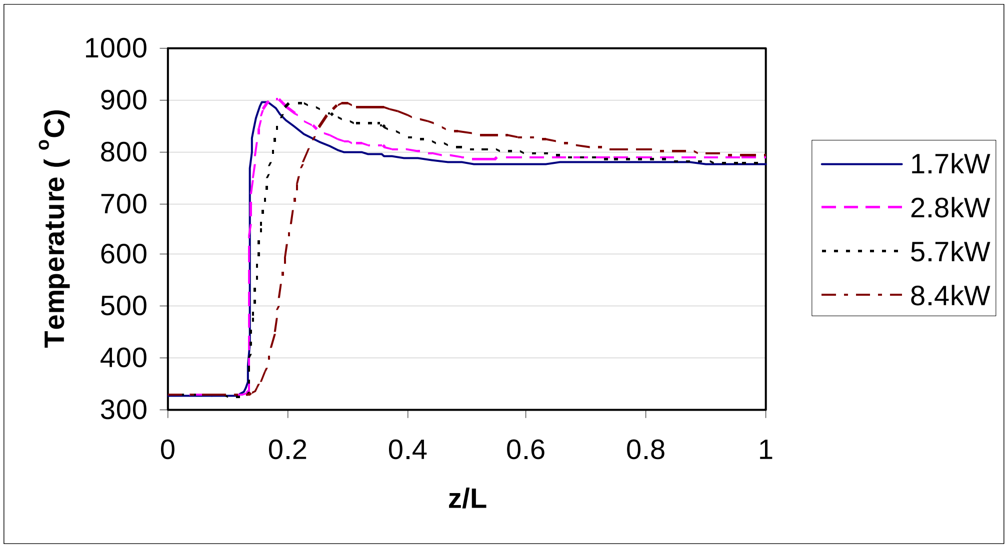

Figure 5.9. Averaged temperature distribution along the dimensionless length of the reactor at various power inputs.

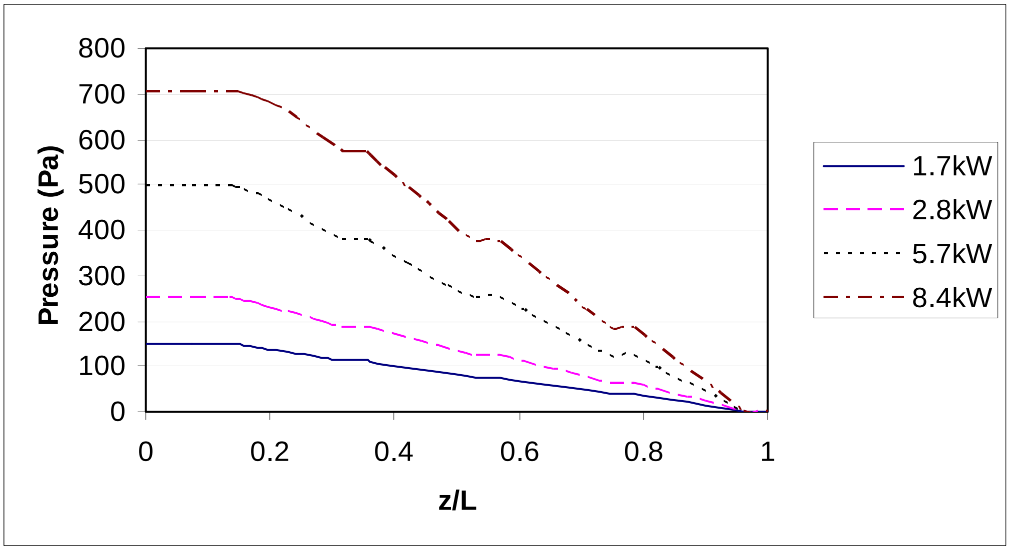

Figure 5.10. Pressure along the dimensionless length of the reactor at various power inputs.

5.3.2 Comparison with Equilibrium Results

Though power input was varied, the mole fraction of products at equilibrium did not change because the mole fraction of reactants at the inlet was held constant. This would be expected since the equilibrium composition is determined only by temperature, pressure, and feed composition. The mole fractions of H_2, CO_2, and CO at equilibrium were the same as the equilibrium values shown in Figure 5.3. The mole fraction of H_2 at the reactor outlet at 1.7 kW was 0.376 (dry basis), and its value at equilibrium was 0.451. Even at the low power input of 1.7 kW, its H_2 yield was still less than that at equilibrium.

CHAPTER 6: CONCLUSIONS

This chapter gives a summary of conclusions drawn from the CFD modeling results.

6.1 CFD Model for Steam Reforming with Iso-Octane Feed

A CFD model of steam reforming was developed and validated using the experimental data of Springmann et al. [45]. A single channel of the monolith reactor was modeled. The reaction mechanisms utilized included both two and three global reactions. The CFD model gave a satisfactory prediction of the mole fraction of H_2 at temperatures of 625 and 675 ˚C. The percentage of deviation from the experimental data was less than 17.7%. This percentage of deviation is adequate for engineering design purposes.

As the inlet H_2O/C molar ratio increased from 2 to 4, the reforming efficiency based on H_2 was around 60%, and the mole fraction of H_2 predicted by the CFD was about 58% of that at the equilibrium. The effect of varying the inlet H_2O/C ratio on the mole fraction of H_2 (wet basis) was small within the simulated conditions. But the mole fraction of H_2 (dry basis) increased with increasing H_2O/C ratio.

The reforming efficiency decreased as the inlet velocity was increased from 2.9 to 5.8 m/s. Further increase of inlet velocity from 5.8 to 8.4 m/s had negligible effect on the reforming efficiency. The difference in reforming efficiency was mainly caused by the steam reforming reaction. The temperature profile was more stretched in the center with increasing inlet velocity.

6.2 CFD Model for Autothermal Reforming with N-Hexadecane Feed

A CFD model of autothermal reforming was developed and validated using the experimental data of Liu et al. [31]. A reaction rate expression was formulated for the reaction of steam reforming to form CO_2 and H_2. The monolith zone was modeled as porous media. Agreement adequate for engineering design purposes was found between the CFD predictions and experimental measurement with respect to the reactor temperature and mole fractions of H_2, CO_2, and CO. The percentage of difference at each comparison point was less than 11.6% for temperature, 16.8% for H_2, 17.3% for CO_2, and 16.0% for CO.

The thermal conductivity of the catalyst support affected the temperature profile in the reactor, but its effect on the mole fractions of H_2, CO_2, and CO in the product was negligible. The maximum temperature predicted in the reactor was decreased about 30 ˚C as the thermal conductivity increased from 2.76 to 202.4 W/m·K.

The increase in power input from 1.7 to 8.4 kW resulted in a decrease in the reforming efficiency. It also affected the profile of mole fractions of products and temperature in the reactor. To achieve similar mole fraction of H_2, the length of the catalytic surface would be longer at a higher power input.

CHAPTER 7: RECOMMENDATIONS

Solid carbon is not included in the current models. Although the amount of solid carbon is usually small in the products, it decreases the activity of the catalyst if it deposits on the catalyst surface. It is difficult to accurately measure the amount of solid carbon through experiments because of its small amount and distribution in the reactor. A future CFD model including solid carbon may be useful in estimating when the deposition of carbon might be important and be useful in screening potential operating conditions.

The modeling results indicate that the reaction chemistry developed in this thesis works well for paraffins, such as iso-octane and n-hexadecane. Partly this is because the reaction rate expressions were based on those from methane. Kang et al. [41] found that the conversion efficiency of aromatics was much lower than that of paraffins with similar carbon number. To simulate reformers which use gasoline or diesel as the fuel, it is expected that reaction rate expressions may be different for non-paraffin hydrocarbons. Thermal cracking of hydrocarbons can happen at temperatures above 600-650 ˚C [52]. Future modeling work may use a mixture of hydrocarbons with appropriate reaction rate expressions and the inclusion of thermal cracking in the reaction mechanism.

To optimize the performance of the fuel cell-based power system, the whole system should be modeled. This suggests that future work may model fuel cells and fuel reformers together to obtain overall system efficiencies.

REFERENCES

[1] Larminie, J., Dicks, A. (2003). Fuel cell systems explained (2nd ed.). West Sussex: John Wiley & Sons.

[2] Prime supplier sales volumes (thousand gallons per day). Energy Information Administration: Washington, DC; 2007. Available at http://tonto.eia.doe.gov/dnav/pet/pet_cons_prim_dcu_nus_a.htm (accessed August 28, 2007).

[3] Krumpelt, M., Krause, T. R., Carter, J. D., Kopasz, J. P., Ahmed, S. (2002). Fuel processing for fuel cell systems in transportation and portable power applications. Catalysis Today, 77, 3–16.

[4] Çengel, Y. A., Boles, M. A. (1998). Thermodynamics: an engineering approach (3rd ed.). New York: McGraw-Hill.

[5] Pettersson, L. J., Westerholm, R. (2001). State of the art of multi-fuel reformers for fuel cell vehicles: problem identification and research needs. International Journal of Hydrogen Energy, 26, 243-264.

[6] Brown, L. F. (2001). A comparative study of fuels for on-board hydrogen production for fuel-cell-powered automobiles. International Journal of Hydrogen Energy, 26, 381-397.

[7] Krummenacher, J. J., West, K. N., Schmidt, L. D. (2003). Catalytic partial oxidation of higher hydrocarbons at millisecond contact times: decane, hexadecane, and diesel fuel. Journal of Catalysis, 215, 332–343.

[8] Pfefferle, L. D. (1995). Heterogeneous/homogeneous reactions and transport coupling for catalytic combustion systems: a review of model alternatives. Catalysis Today, 26, 255-265.

[9] Kolaczkowski, S. T. (1999). Modelling catalytic combustion in monolith reactors - challenges faced. Catalysis Today, 47, 209–218.

[10] Pacheco, M., Jorge, S., Kopasz, J. (2003). Reaction kinetics and reactor modeling for fuel processing of liquid hydrocarbons to produce hydrogen: isooctane reforming. Applied Catalysis. A, General, 250, 161-175.

[11] Schlichting, H., Gersten, K. (2000). Boundary layer theory, Berlin: Springer.

[12] Coltrin, M. E., Moffat, H. K., Kee, R. J., Rupley, F. M. (1993). CRESLAF (Version 4.0): A Fortran program for modeling laminar, chemically reacting, boundary-layer flow in cylindrical or planar channels. Sandia National Laboratories Report SAND93-0478.

[13] Raja, L. L., Kee, R. J., Deutschmann, O., Warnatz, J., Schmidt, L. D. (2000). A critical evaluation of Navier–Stokes, boundary-layer, and plug-flow models of the flow and chemistry in a catalytic-combustion monolith. Catalysis Today, 59, 47–60.

[14] Deutschmann, O., Schwiedernoch, R., Maier, L. I., Chatterjee, D. in: Iglesia, E., Spivey, J. J., Fleisch T. H. (Eds.), (2001). Natural Gas Conversion VI, Studies in Surface Science and Catalysis, Elsevier, Amsterdam, 215–258.

[15] Mazumder, S., Sengupta, D. (2002). Sub-Grid scale modeling of heterogeneous chemical reactions and transport in full-scale catalytic converters. Combustion and Flame, 131, 85–97.

[16] Giroux, T., Hwang, S., Liu, Y., Ruettinger, W., Shore, L. (2005). Monolithic structures as alternatives to particulate catalysts for the reforming of hydrocarbons for hydrogen generation. Applied Catalysis B: Environmental, 56, 95–11.

[17] Deutschmann, O. Detailed Chemistry in CFD. Available at http://www.detchem.com/mechanisms/ (accessed August 28, 2007).

[18] De Groote, A. M., Froment, G. F. (1996). Simulation of the catalytic partial oxidation of methane to synthesis gas. Applied Catalysis. A, General, 138, 245-264.

[19] Hoang, D. L., Chan, S. H. (2004). Modeling of a catalytic autothermal methane reformer for fuel cell applications. Applied Catalysis. A, General, 268, 207-216.

[20] Papadias, D., Lee, S. H. D., Chmielewski, D. J. (2006). Autothermal reforming of gasoline for fuel cell applications: A transient reactor model. Industrial & Engineering Chemistry Research, 45, 5841-5858.

[21] Lattner, J. R., Harold, M. P. (2004). Comparison of conventional and membrane reactor fuel processors for hydrocarbon-based PEM fuel cell systems. International Journal of Hydrogen Energy, 29, 393-417.

[22] Xu, J., Froment, G. F. (1989). Methane steam reforming, methanation and water-gas shift: I. intrinsic kinetics. AIChE Journal, 35, 88-96.

[23] Numaguchi, T., Kikuchi, K. (1988). Intrinsic kinetics and design simulation in a complex reaction network: steam-methane reforming. Chemical Engineering Science, 43, 2295–2301.

[24] de Smet, C. R. H., de Croon, M. H. J. M., Berger, R. J., Marin, G. B., Schouten, J. C. (2001). Design of adiabatic fixed-bed reactors for the partial oxidation of methane to

synthesis gas. Application to production of methanol and hydrogen-for-fuel-cells. Chemical Engineering Science, 56, 4849–4861.

[25] Trimm, D. L., Lam, C-W. (1980). The combustion of methane on platinum-alumina fibre catalysts—I. Kinetics and mechanism. Chemical Engineering Science, 35, 1405–1413.

[26] Ma, L., Trimm, D. L., Jiang, C. (1996). The design and testing of an autothermal reactor for the conversion of light hydrocarbons to hydrogen I. the kinetics of the catalytic oxidation of light hydrocarbons. Applied catalysis. A: General, 138, 275-283.

[27] Ibrahim, H. H., Idem, R. O. (2006). Kinetic studies of the partial oxidation of isooctane for hydrogen production over a nickel-alumina catalyst. Chemical Engineering Science, 61, 5912-5918.

[28] Wang, X., Gorte, R. J. (2003). The effect of Fe and other promoters on the activity of Pd/ceria for the water-gas shift reaction. Applied Catalysis. A, General, 247, 157-162.

[29] Grenoble, D. C., Estadt, M. M., Ollis, D. F. (1981). The chemistry and catalysis of the water gas shift reaction. 1. The kinetics over supported metal-catalysts. Journal of Catalysis, 67, 90-102.

[30] Wheeler, C., Jhalani, A., Klein, E. J., Tummala, S., Schmidt, L. D. (2004). The water–gas-shift reaction at short contact times. Journal of Catalysis, 223, 191–199.

[31] Liu, D. J., Kaun, T. D., Liao, H. K., Ahmed, S. (2004). Characterization of kilowatt-scale autothermal reformer for production of hydrogen from heavy hydrocarbons. International Journal of Hydrogen Energy, 29, 1035-1046.

[32] Veser, G., Frauhammer, J. (2000). Modelling steady state and ignition during catalytic methane oxidation in a monolith reactor. Chemical Engineering Science, 55, 2271-2286.

[33] Canu, P., Vecchi, S. (2002). CFD simulation of reactive flows: catalytic combustion in a monolith. AIChE Journal, 48, 2921-2935.

[34] Chaniotis, A. K., Poulikakos, D. (2006). Modeling and optimization of catalytic partial oxidation methane reforming for fuel cells. Journal of Power Sources, 142, 184-193.

[35] Hecht, E. S., Gupta, G. K., Zhu, H., Dean, A., Kee, R. J., Maier, L., Deutschmann, O. (2005). Methane reforming kinetics within a Ni–YSZ SOFC anode support. Applied Catalysis. A, General, 295, 40–51.

[36] Quiceno, R., Perez-Ramirez, J., Warnatz, J., Deutschmann, O. (2006). Modeling the high-temperature catalytic partial oxidation of methane over platinum gauze: detailed gas-phase and surface chemistries coupled with 3D flow field simulations. Applied Catalysis. A, General, 303, 166-176.

[37] Ahmed, S., Ahluwalia, R., Lee, S. H. D., Lottes, S. (2006). A gasoline fuel processor designed to study quick-start performance. Journal of Power Sources, 154, 214–222.

[38] Stutz, M. J., Poulikakos, D. (2005), Effects of microreactor wall heat conduction on the reforming process of methane. Chemical Engineering Science, 60, 6983-6997.

[39] Schwiedernoch, R., Tischer, S., Correa, C., Deutschmann, O. (2003). Experimental and numerical study on the transient behavior of partial oxidation of methane in a catalytic, monolith. Chemical Engineering Science, 58, 633–642.

[40] Cheekatamarla, P. K., Lane, A. M. (2005). Catalytic autothermal reforming of diesel fuel for hydrogen generation in fuel cells I. Activity tests and sulfur poisoning. Journal of Power Sources, 152, 256–263.

[41] Kang, I., Bae, J., Bae, G. (2006), Performance comparison of autothermal reforming for liquid hydrocarbons, gasoline and diesel for fuel cell applications. Journal of Power Sources, 163, 538–546.

[42] Mengel, C., Konrad, M., Wruck, R., Lucka, K., Köhne, H. (2008). Diesel steam reforming for PEM fuel cells. Journal of Fuel Cell Science and Technology, 5, 021005-1-5.

[43] Kolb, G., Baier, T., Schűrer, J., Tiemann, D., Ziogas, A., Ehwald, H., Alphonse, P. (2008). A micro-structured 5 kW complete fuel processor for iso-octane as hydrogen supply system for mobile auxiliary power units Part I. Development of autothermal reforming catalyst and reactor. Chemical Engineering Journal, 137, 653–663.

[44] Lindermeir, A., Kah, S., Kavurucu, S., Mühlner, M. (2007). On-board diesel fuel processing for an SOFC-APU — Technical challenges for catalysis and reactor design. Applied Catalysis. B, Environmental, 70, 488-497.

[45] Springmann, S., Friedrich, G., Himmen, M., Sommer, M., Eigenberger, G. (2002). Isothermal kinetic measurements for hydrogen production from hydrocarbon fuels using a novel kinetic reactor concept. Applied Catalysis. A, General, 235, 101–111.

[46] Shi, L., Bayless, D. J., Prudich, M. (2008). A model of steam reforming of iso-octane: The effect of thermal boundary conditions on hydrogen production and reactor temperature. International Journal of Hydrogen Energy, 33, 4577–4585.

[47] Fluent, Inc. (2006). FLUENT 6.3 User's Guide. Lebanon, NH.

[48] Aparicio L. M. (1997). Transient isotopic studies and microkinetic modeling of methane reforming over nickel catalysts. Journal of Catalysis, 165, 262-274.

[49] Tiemersma T. P., Patil C. S., van Sint Annaland M., Kuipers, J. A. M. (2006). Modelling of packed bed membrane reactors for autothermal production of ultrapure hydrogen. Chemical Engineering Science, 61, 1602 – 1616.

[50] Aspen Technology, Inc. (2005). AspenONE user guide. Cambridge, MA.

[51] Shi L., Bayless D. J. (2008). Analysis of jet fuel reforming for solid oxide fuel cell applications in auxiliary power units. International Journal of Hydrogen Energy, 33, 1067-1075.

[52] Rostrup-Nielsen, J. R., Sehested, J. (2002). Hydrogen and synthesis gas by steam- and CO_2 reforming. Advanced Catalysis. 47, 65-139.

APPENDIX A: UDF USED IN THE MODEL OF STEAM REFORMING

```
/*User-defined function used in the model of steam reforming*/

#include "udf.h"

DEFINE_SR_RATE(my_rate,f,t,r,mw,yi,rr)
{
      Thread *t0=THREAD_T0(t);
      cell_t c0=F_C0(f,t);

      /*mass fraction of species i at the wall*/
      real y_c8h18=yi[0];
      real y_h2o=yi[1];
      real y_h2=yi[2];
      real y_co=yi[3];
      real y_co2=yi[4];
      real y_n2=yi[5];
      real Nsum, R, A1, A2, E1, E2, k1, k2, Keq1, Keq2, T_w, TP,
r1,r2,min,max;

      min=0;
      max =1e+5;
      /*calculate species i in the unit of kgmol i/kg mix*/
      y_c8h18 *= 1/mw[0];
      y_h2o *= 1/mw[1];
      y_h2 *= 1/mw[2];
      y_co *= 1/mw[3];
      y_co2 *= 1/mw[4];
      y_n2 *= 1/mw[5];
      /*total mole number per kg mix */
      Nsum = y_c8h18 + y_h2o + y_h2 + y_co + y_co2 + y_n2;

      /*calculate mole fraction of species i in the unit of kgmol
i/kgmol mix*/
      y_c8h18 *= 1/Nsum;
      y_h2o *= 1/Nsum;
      y_h2 *= 1/Nsum;
      y_co *= 1/Nsum;
      y_co2 *= 1/Nsum;
      y_n2 *= 1/Nsum;

      /*gas constant, J/molK */
      R=8.314;
      /*equilibrium constant calculated by the empirical formula*/
      T_w=F_T(f,t);
      Keq1=8.1e+6*pow(T_w,3.03)/exp(2.023e+5/R/T_w);
      Keq2=9.01e-6*pow(T_w,0.968)*exp(4.36e+4/R/T_w);
      /*reaction rate constant, need to be guessed, trial-and-error*/
      A1=1.4e+11, A2=25.;
      E1=2.401e+5, E2=6.71e+4;  /*J/mol*/
      k1=A1/exp(E1/R/T_w);
      k2=A2/exp(E2/R/T_w);
```

```
      /*total pressure in the cell near wall, bar*/
      TP=C_P(c0,t0)/1.0e+5;

      if(STREQ(r->name, "reaction-1")){
            /*unit for rr, kgmol/m2s*/
            r1= k1*(TP*y_c8h18-
pow(TP*y_h2,3)*y_co/(y_h2o*Keq1))/pow(TP*y_h2o,0.6);
            if(r1 < min){
            *rr = min;
            }
            else if (r1 > min && r1 < max)
                  *rr = r1;
            else if (r1 > max){
                  *rr = max;
            }
      }
      else if (STREQ(r->name, "reaction-2")){
            r2= k2*TP*(y_co-y_h2*y_co2/(y_h2o*Keq2));
            if(r2 < min){
            *rr = min;
            }
            else if (r2 > min && r2 < max)
                  *rr = r2;
            else if (r2 > max){
                  *rr = max;
            }
      }
}
```

APPENDIX B: UDF USED IN THE MODEL OF AUTOTHERMAL REFORMING

```
/*User-defined function used in the model of autothermal reforming.
Surface reaction in porous media, only a quarter of the geometry
modeled*/

#include "udf.h"

DEFINE_SR_RATE(my_rate,f,t,r,mw,yi,rr)
{
      /*mass fraction of species i at the wall*/
      real y_c16h34=yi[0];
    real y_o2=yi[1];
      real y_h2o=yi[2];
      real y_h2=yi[3];
      real y_co=yi[4];
      real y_co2=yi[5];
      real y_n2=yi[6];
      real Nsum, R, A1, A2, A3, A4,E1, E2, E3, E4,k1, k2, k3, k4,Kef,
Keo, Keq2, Keq3, Keq4;
      real T,rt, TP, r1,r2,r3, r4, min, mino, max,a,b;

      min = -100;
      mino = 0;
      max = 100;
      /*calculate species i in the unit of kgmol i/kg mix*/
      y_c16h34 *= 1/mw[0];
    y_o2 *= 1/mw[1];
      y_h2o *= 1/mw[2];
      y_h2 *= 1/mw[3];
      y_co *= 1/mw[4];
      y_co2 *= 1/mw[5];
      y_n2 *= 1/mw[6];
      /*total mole number per kg mix */
      Nsum = y_c16h34 + y_o2 + y_h2o + y_h2 + y_co + y_co2 + y_n2;

      /*calculate mole fraction of species i in the unit of kgmol
i/kgmol mix*/
      y_c16h34 *= 1/Nsum;
    y_o2 *= 1/Nsum;
      y_h2o *= 1/Nsum;
      y_h2 *= 1/Nsum;
      y_co *= 1/Nsum;
      y_co2 *= 1/Nsum;
      y_n2 *= 1/Nsum;

      /*gas constant, J/molK */
      R=8.314;
      /*equilibrium constant calculated by the empirical formula*/
      T=C_T(f,t);
      rt=R*T;
      Kef=0.126*exp(27300/rt); /*Equalibrium constant for C16H34
adsorption*/
```

```
      Keo=7.87e-7*exp(92800/rt); /*Equalibrium constant for O2
adsorption*/
      Keq2=8.1e+6*pow(T,3.03)/exp(2.023e+5/rt);
      Keq3=9.01e-6*pow(T,0.968)*exp(4.36e+4/rt);
    Keq4=4.926e+5*pow(T,2.85)/exp(1.6638e+5/rt);

      /*reaction rate constant, need to be guessed, trial-and-error*/
      A1=8.11e+6, A2=9.69e+7, A3=2.5,A4=1.0e+9;
      E1=8.6e+4, E2=2.401e+5, E3=5.45e+4, E4=2.439e+5;  /*J/mol*/
      k1 = A1/exp(E1/rt); /*for reaction C16H34+24.5O2 ->16CO2+17H2O */
    k2 = A2/exp(E2/rt); /*for reaction C16H34 + 16H2O <->16CO + 33H2 */
      k3 = A3/exp(E3/rt); /*for reaction CO + H2O <->CO2 + H2 */
    k4 = A4/exp(E4/rt); /*for reaction C16H34 + 32 H2O <-> 16 CO2 + 49
H2 */

      /*total pressure in the cell near wall, bar*/
      TP=C_P(f,t)/1.0e+5;

      if(FLUID_THREAD_P(t) && THREAD_VAR(t).fluid.porous){
        if(STREQ(r->name, "reaction-1")){
        /*unit for rr, kgmol/m2s*/

      r1=k1*TP*y_c16h34*pow(TP*y_o2,0.5)/pow((1+Kef*TP*y_c16h34+Keo*pow
(TP*y_o2,0.5)),2);
        if(r1 < mino){
            *rr = mino;
            }
            else if (r1 > mino && r1 < max)
                  *rr = r1;
            else if (r1 > max){
                  *rr = max;
            }
            }
            else if (STREQ(r->name, "reaction-2")){
            r2= k2*(TP*y_c16h34-
pow(TP*y_h2,3)*y_co/(y_h2o*Keq2))/pow(TP*y_h2o,0.6);
            if(r2 < min){
            *rr = min;
            }
            else if (r2 > min && r2 < max)
                  *rr = r2;
            else if (r2 > max){
                  *rr = max;
            }
            }
            else if (STREQ(r->name, "reaction-3")){
            r3= k3*TP*(y_co-y_h2*y_co2/(y_h2o*Keq3));
            if(r3 < min){
            *rr = min;
            }
            else if (r3 > min && r3 < max)
                  *rr = r3;
            else if (r3 > max){
                  *rr = max;
```

```
            }
            }
            else if (STREQ(r->name, "reaction-4")){
          r4= k4*(TP*y_c16h34-
pow(TP*y_h2,4)*TP*y_co2/(pow(TP*y_h2o,2)*Keq4))/pow(TP*y_h2o,0.3);
          if(r4 < min)
            *rr = min;
            else if (r4 > min && r4 < max)
                  *rr = r4;
            else if (r4 > max)
                  *rr = max;
            }
      }
}
```

TAD
Servi
ces